Cavendish–HEP–97/01
January 1997

The processes $e^+e^- \rightarrow b\bar{b}W^\pm H^\mp$ and $e^+e^- \rightarrow b\bar{b}H^+H^-$ at the Next Linear Collider in the Minimal Supersymmetric Standard Model

Stefano Moretti[1] and Kosuke Odagiri[1]

Cavendish Laboratory, University of Cambridge,
Madingley Road, Cambridge, CB3 0HE, United Kingdom.

Abstract

The complete matrix elements for $e^+e^- \rightarrow b\bar{b}W^\pm H^\mp$ and $e^+e^- \rightarrow b\bar{b}H^+H^-$ are computed at tree-level within the Minimal Supersymmetric Standard Model. Rates of interest to phenomenological analyses at the Next Linear Collider are given. In particular, we analyse: (i) $t\bar{t}$ pair production followed by the top decays into $b\bar{b}W^\pm H^\mp$ and $b\bar{b}H^+H^-$ final states; (ii) H^+H^- signals in which $H^\pm \rightarrow hW^\pm \rightarrow b\bar{b}W^\pm$ and $H^\pm \rightarrow tb \rightarrow b\bar{b}W^\pm$. Top and Higgs finite width effects are included as well as all those due to the irreducible backgrounds.

[1]E-mails: moretti,odagiri@hep.phy.cam.ac.uk

1. Introduction

In the present paper we intend to conclude a long-term project of computing effects due to the finite width of the unstable particles as well as to the non-resonant diagrams entering in electroweak (EW) processes of the type

$$e^+e^- \to b\bar{b}X^+X^-, \tag{1}$$

where $X^\pm = W^\pm, H^\pm$, within the Standard Model ($\mathcal{SM}$) and the Minimal Supersymmetric Standard Model ($\mathcal{MSSM}$) at Next Linear Collider (NLC) energies [1]. The case $X^+X^- \equiv W^+W^-$ within the $\mathcal{SM}$ was considered in Refs. [2, 3] (see also Ref. [4]) whereas the equivalent process in the $\mathcal{MSSM}$ was discussed in Ref. [5][2].

By the time that an NLC machine will be operating, m_t will already be known precisely and either M_ϕ will have been measured or a large part of the $\mathcal{MSSM}$ parameter space $(M_A, \tan\beta)$ defining the values of $M_{\rm Higgs}$ will have already been explored[3], thanks to the experiments at the Tevatron [7], LEP2 [8] and LHC [9, 10]. (For an illustration of the discovery potential of such machines, we refer the reader to [7, 8, 9, 10].) Anyhow, whichever the status of the measurements of m_t, M_H, M_h, M_A and/or $M_{H^\pm}$ will be, we would like to stress that detailed studies of both top quark and Higgs boson properties (other than the mass, e.g., the width, the branching ratios, etc.) will more easily be carried out at an e^+e^- linear accelerator, operating in the energy range $2m_t \lesssim \sqrt{s} \lesssim 1$ TeV. At such a machine, the absence of the huge QCD background typical of hadron colliders combined with the large luminosity and 'effective' centre-of-mass (CM) energy available allows one to cover the whole of the Higgs mass range and to exploit all possible Higgs and top decay channels in order to perform very high precision measurements of their parameters.

Top and Higgs signatures naturally enter in processes of the type (1). In fact, in the $\mathcal{SM}$, the process $e^+e^- \to b\bar{b}W^+W^-$ is a signature of both top quark production in $t\bar{t}$ pairs and Higgs boson bremsstrahlung in the $Z\phi$ channel. On the one hand, top pairs produced via the $e^+e^- \to t\bar{t}$ decay through $t\bar{t} \to b\bar{b}W^+W^-$ whereas, on the other hand, the channel $Z\phi \to b\bar{b}W^+W^-$ will be one of the cleanest ways of detecting a heavy Higgs, thanks to the high performances expected from the vertex detectors in triggering b-quarks [11][4]. Within the $\mathcal{MSSM}$, the reaction $e^+e^- \to b\bar{b}W^+W^-$ allows one to study not only the Supersymmetric counterparts of the two mentioned $\mathcal{SM}$ processes[5], but also AH production followed by $A \to b\bar{b}$ and $H \to W^+W^-$ as well as hW^+W^- in which $h \to b\bar{b}$ [5].

It is the purpose of this note to consider the last two possibilities left within the $\mathcal{MSSM}$, that is

$$e^+e^- \to b\bar{b}W^\pm H^\mp, \tag{2}$$

$$e^+e^- \to b\bar{b}H^+H^-. \tag{3}$$

[2]For the case of the irreducible background from QCD in $W^\pm + 4$jet events, see Ref. [6].

[3]Here and in the following, ϕ indicates the Higgs boson of the $\mathcal{SM}$ whereas the subscript 'Higgs' refers collectively to the $H, h, A, H^\pm$ scalars of the $\mathcal{MSSM}$.

[4]The branching ratio (BR) of the channel $Z \to b\bar{b}$ is five times larger than that into $\mu^+\mu^-$ or e^+e^- and it is free from backgrounds due to $W^\pm$ decays.

[5]In case of Higgs production, the heaviest of the $\mathcal{MSSM}$ neutral Higgses (i.e., H) replacing the $\mathcal{SM}$ Higgs scalar (i.e., ϕ).

As it was done in the previous publications [2]–[5], our aim is twofold.

- Firstly, to establish the importance of top finite width effects and of those due to the non-resonant background in case of $t\bar{t} \to b\bar{b}W^{\pm}H^{\mp}$ and $t\bar{t} \to b\bar{b}H^{+}H^{-}$ decays.
- Secondly, to study Higgs signatures, such as $e^{+}e^{-} \to H^{+}H^{-}$ production followed by the decay of one of the charged Higgses into:

1. $h^{*}W^{\pm *} \to b\bar{b}W^{\pm *}$ and
2. $t^{*}b \to b\bar{b}W^{\pm}$ (if $m_t \lesssim M_{H^{\pm}} - m_b$),

   where the asterisk indicates possible off-shell channels. Note that these two signatures are produced via process (2). We further notice that the top-antitop decay channels
3. $t\bar{t} \to b\bar{b}W^{\pm}H^{\mp}$ and $t\bar{t} \to b\bar{b}H^{+}H^{-}$

   represent themselves a source of $H^{\pm}$ signals.

Although all the topologies yielding $b\bar{b}W^{\pm}H^{\mp}$ and $b\bar{b}H^{+}H^{-}$ final states produce Higgs bosons (both charged an neutral), we will consider the corresponding diagrams as (irreducible) 'background' to the two 'signals' $e^{+}e^{-} \to t\bar{t}$ and $e^{+}e^{-} \to H^{+}H^{-}$, as the former represent Higgs production mechanisms that are largely suppressed with respect to the latter and also to others exploited in neutral Higgs boson searches (for a review of these see, e.g., Ref. [12])[6]. Furthermore, it is worth reminding the reader that, at least over the areas of the $\mathcal{MSSM}$ parameter space where the $t \to bH^{+}$ and $H^{+} \to hW^{+} \to b\bar{b}W^{+}$ decay modes are both important (see later on), the processes $e^{+}e^{-} \to t\bar{t}$ and $e^{+}e^{-} \to H^{+}H^{-}$ cannot be unambiguously separated and studied independently. Therefore, in such $(M_A, \tan\beta)$ regions, any of the two reactions constitutes an irreducible background to the other. The different topologies contributing at leading order to processes (2)–(3) are given in Figs. 1a and 1b, respectively. In the first case they lead to 51 different Feynman diagrams whereas for the second case the number is 60.

For future reference, we also present in Fig. 1c the $\mathcal{MSSM}$ BRs of top quarks and charged Higgs bosons in the $M_{H^{\pm}}$ range and for the values of $\tan\beta$ that will be used in our analysis. Note that such rates dictate the decay phenomenology of the top (diagrams 2 in Fig. 1a and 3 in Fig. 1b) and Higgs (diagrams 9 and 12 in Fig. 1a) signals that will be studied later on. As in our forthcoming discussions we will interchange the rôle of $M_{H^{\pm}}$ and M_A, we have plotted both these quantities as mass scales in Fig. 1c.

The plan of the paper is as follows. In the next Section we describe the calculations we have performed. In Section 3 we present our results. Our conclusions are given in Section 4.

[6] We notice that such diagrams are nonetheless interesting on their own, e.g., as a way of testing the gauge structure of Higgs sector of the $\mathcal{MSSM}$, as they involve many of the fundamental tree-level vertices of the theory. This is however beyond the scope of this study.

2. Matrix Elements

To compute the Matrix Elements (MEs) of processes (2)–(3) we have used helicity amplitude techniques. A first code has been produced by using the method of Ref. [13]. This has then been checked against a second one built up by resorting to the subroutines contained in the package HELAS [14]. In particular, in order to implement the diagrams of Figs. 1a–b, we have made use of the subroutines involving scalars with the vertices and propagators appropriately arranged to reproduce the interactions and wave-functions of the five Higgses in the unitary gauge of the $\mathcal{MSSM}$.

The two `FORTRAN` codes have been programmed by the two authors independently and they agree at amplitude squared level within 12 significative digits in `REAL*8` precision. Moreover, all the amplitudes produced with the first method have been tested for gauge invariance by computing the two MEs in other two gauges as well (i.e., the Feynman and the Landau ones). In order to deal with the complicated resonant structure of processes (2)–(3), we have adopted the technique of splitting the two MEs in a sum of non-gauge-invariant pieces, each of these implementing a different resonant structure, and of integrating them separately with the appropriate mapping of the phase space variables. Such a procedure has already been documented in detail for the case of the $e^+e^- \to b\bar{b}W^+W^-$ process in the $\mathcal{SM}$ in Ref. [3], so we only sketch out here the method.

Firstly, one isolates the diagrams with similar resonant structure by grouping these together in 'subamplitudes'. For example, one can recognise in process (2) the resonances: $t\bar{t} \to (bW^+)(\bar{b}H^-)$, $t \to bW^+$, $\bar{t} \to \bar{b}H^-$, $H, h, A, Z \to b\bar{b}$, $H^+H^- \to (t\bar{b})H^- \to (b\bar{b}W^+)H^-$ and $H^+H^- \to (hW^+)H^- \to (b\bar{b}W^+)H^-$. In case of reaction (3) one has the following Breit-Wigner peaks: $t\bar{t} \to (bH^+)(\bar{b}H^-)$, $t \to bH^+$, $\bar{t} \to \bar{b}H^-$ and $H, h, A, Z \to b\bar{b}$. Secondly, one defines the mentioned non-gauge-invariant components of the amplitudes squared, by appropriately combining the subamplitudes. For example, in both processes (2)–(3) we have simply taken the square of the various resonant subamplitudes (yielding 9 and 7 terms, respectively) whereas we have combined their interferences altogether in the last term, apart from those between the two single-top and the only double-top channels, which were added to the t- and $\bar{t}$-diagrams in both reactions (2)–(3). Thirdly, one maps the phase spaces around the resonances. For example, for our analysis this was made by performing the change of variable

$$Q^2 - M^2 = M\Gamma\tan\theta, \longrightarrow dQ^2 = \frac{(Q^2-M^2)^2 + M^2\Gamma^2}{M\Gamma} d\theta \tag{4}$$

(where Q, M, Γ stand for the virtuality, the mass and the width of the resonance), which gives integrands smoothly dependent on θ. Fourthly, the various amplitude squared terms are integrated separately (we have used VEGAS [15] to this purpose) and added up in the end (to recover gauge invariance). We however notice that, if taken separately, these terms provide a useful way of looking inside the processes and distinguishing between the different fundamental interactions.

Concerning the values adopted for the $\mathcal{SM}$ and $\mathcal{MSSM}$ parameters and the relations implemented for the $\mathcal{MSSM}$ Higgs masses and couplings we refer to Refs. [2]–[5]. Furthermore, as in the previous publications [2]–[5], we have chosen here, as representative for $\tan\beta$, the two extreme values 1.5 and 30. M_A varies between 50 and 220

GeV, as higher values would be uninteresting in the present context (the corresponding rates for both the $t \to bH^\pm$ decays and the H^+H^- pair production become heavily suppressed). Following the latest measurements at FNAL [16], the top mass has been set equal to 174 GeV. Therefore, we use as indicative of the top-antitop threshold energy the value $\sqrt{s} = 350$ GeV, along with the final stage energy of 500 GeV.

Our calculations have been carried out at leading order only. We have not included beamsstrahlung and bremsstrahlung effects either. We are however confident that such approximations will not spoil our conclusions. Indeed, it has been proved that this is true for the process $e^+e^- \to b\bar{b}W^+W^-$ [2, 5] and we expect the same in the present context.

A final consideration is now in order. Following the approach of Refs. [2]–[5], we have generally kept the final state bosons $W^\pm$ and $H^\pm$ on-shell in our computations. However, we made an exception in one case: when computing the squared of graph 12 of Fig. 1a. This represents the Higgs signal $e^+e^- \to H^+H^-$ in which one of the two scalars decays into $hW^\pm$ pairs, followed by $h \to b\bar{b}$. That is, when only the light neutral Higgs is allowed to be off-shell. However, this channel is relevant in the case of off-shell $W^\pm$ bosons as well. Therefore, in order to keep this into account, when calculating the contribution of the mentioned diagram to the total cross section of process (2) we have attached a fermion-antifermion decay current to the $W^\pm$ boson and computed the amplitude squared of a 2$\to$5 process. Indeed, proceeding this way, the rates that we calculated from the integration of this diagram over the appropriate phase space reproduce rather accurately those obtained by multiplying the cross section for $e^+e^- \to H^+H^-$ [12] times the off-shell BR[$H^\pm \to hW^\pm \to b\bar{b}$jj] [17], where j represents a jet (see next Section).

3. Results

In carrying out our analysis we closely follow Refs. [2, 3, 5] and the studies reported in the Sections 'Higgs Particles' and 'Top Quark Physics' of Ref. [1]. Furthermore, throughout this paper we assume that the mass scale of the Supersymmetric partners of ordinary matter is beyond the energy reach of the NLC, so that they cannot be produced at such a collider. In particular, we neglect considering the Supersymmetric decay $t \to \tilde{t}\tilde{\chi}^0_1$, where $\tilde{t}$ refers to the stop and $\tilde{\chi}^0_1$ is the lightest neutralino, as well as other possible $\mathcal{MSSM}$ modes[7] [19].

3.1 Event selection

In our selection strategy we assume a six-particle semi-leptonic(hadronic) tagging, for both reactions (2)–(3): that is, b's are assumed to hadronise whereas one of the charged bosons decays into jet-jet pairs and the other into $\tau\nu_\tau$. In this way, the selected final state is always made up by a high energy and isolated τ accompanied by a multi-hadronic system and appreciable missing four-momentum.

[7] For a recent review of the latter, see Ref. [18].

$e^+e^- \to b\bar{b}W^\pm H^\mp$

This means that in events of the type (2) one can in principle pick up a tau-lepton either from a $W^\pm$ or a $H^\pm$. However, it should be noticed that the four-momentum of the tagged boson is eventually reconstructed by summing that of the decay lepton to the missing one (the latter being computed using the kinematic constraints [19])[8]. Therefore, one can always ask that the invariant mass of the lepton-neutrino system is larger than $\sqrt{M^2_{W^\pm} + M^2_A} \approx 100$ GeV to remove $W^\pm \to \tau\nu$ decays, $M_A \approx 60$ GeV being the lower experimental limit on the mass of the pseudoscalar neutral Higgs of the $\mathcal{MSSM}$ [20]. This way, we explicitly require only hadronic $W^\pm$ decays in process (2). This has a clear advantage: in fact, it allows one to easily reconstruct resonant invariant mass spectra (i.e., $M_{bW^\pm \to b\mathrm{jj}}$ for the top and $M_{b\bar{b}W^\pm \to b\bar{b}\mathrm{jj}}$ for the charged Higgs). In addition, the hadronic channels represent the largest fraction of the total $W^\pm$ decay rate (around 70%). We also believe the selection of the channel $H^\pm \to \tau\nu_\tau$ in reaction (2) not restrictive in the present context, for two reasons. On the one hand, the tau-neutrino channel is always sizeable up to $M_{H^\pm} \approx 170 - 180$ GeV (i.e., the tb decay threshold) and for all $\tan\beta$'s. [17]. Therefore, when tagging semi-leptonically(hadronically) over this $M_{H^\pm}$ range one naturally retains a large part of the original top (diagram 2 in Fig. 1a) and Higgs (diagram 12 in Fig. 1a) events. Indeed, it should be noticed that only charged Higgses with mass up to 161 GeV or so (corresponding to $M_A \approx 140$ GeV) can be produced with detectable rate at $\sqrt{s} = 350$ GeV via $e^+e^- \to H^+H^-$. On the other hand, when $M_{H^\pm} \gtrsim 180$ GeV (thus when $\sqrt{s} = 500$ GeV), top quarks mainly decay via the $bW^\pm$ channel so that $e^+e^- \to t\bar{t}$ events are in practise accounted for by the $e^+e^- \to b\bar{b}W^+W^-$ channel alone [2, 5]. In addition, we remark that double t- and/or h-decays $H^+H^- \to b\bar{b}t\bar{t}, tbhW^\pm, hhW^+W^- \to b\bar{b}b\bar{b}W^+W^-$ of charged Higgses produced via $e^+e^- \to H^+H^-$ would yield a final signature with numerous hadronic tracks (e.g., up to 8 jets can be produced, if $W^+W^- \to \mathrm{jjjj}$!) with the consequent problems due to the combinatorics, so that to tag one of the Higgses via the lepton-neutrino channel might be a better approach[9]. For example, for large $\tan\beta$ values, the $H^\pm \to \tau\nu_\tau$ channel has a BR that is always larger than ≈ 0.35 [17] for the values of $H^\pm$ masses that can be produced at $\sqrt{s} = 500$ GeV (say, up to $M_{H^\pm} \approx 235$ GeV, that is, for $M_A \lesssim 220$ GeV). In contrast, if $\tan\beta$ is small, the heavy mass region $M_{H^\pm} \gtrsim m_t$ is clearly sacrificed by requiring one of the $H^\pm$'s to decay into $\tau\nu$ pairs [17], so that in such a case the mentioned multi-hadronic final states will necessarily need to be exploited in experimental analyses.

$e^+e^- \to b\bar{b}H^+H^-$

In the case of reaction (3) one is only interested in top decays (diagram 3 of Fig. 1b), since $H^\pm$ events cannot be produced at large rate by any of the other diagrams. There-

[8]This is exactly true only when the energy of the colliding electron/positron beams is known (i.e., no Linac energy spread, bremsstrahlung and beamsstrahlung), when the detector is ideal (i.e., infinite resolution and complete geometrical coverage) and when no other neutrino from cascade decays is present in the interaction. In a more realistic case, corrections have to be made to account for all the above effects, which in fact do not spoil the effectiveness of the method [19].

[9]Alternatively, such multi-hadronic channels would need a proper simulation (including hadronisation, detector effects, etc.) which is clearly beyond the intention of this study.

fore, in this case, the relevant charged Higgs masses are those for which $M_{H^\pm} < m_t - m_b$ and strictly below the top-bottom threshold the $\tau\nu_\tau$ channel is the dominant one at all $\tan\beta$'s [17]. In these conditions then, a purely leptonic decay channel might seem more appropriate: i.e., $t\bar{t} \to b\bar{b}H^+H^- \to b\bar{b}\tau^+\tau^-\nu_\tau\bar{\nu}_\tau$. However, we do not consider here this possibility. Firstly, because it would prevent one from reconstructing invariant mass top/Higgs spectra and, secondly, because over the experimentally allowed $\tan\beta$ range (say, between 1 and 40) the $t \to bH^\pm$ decays are always suppressed compared to the $t \to bW^\pm$ ones [21], so that the $t\bar{t} \to b\bar{b}W^\pm H^\mp$ channel represents a better option anyway to detect charged Higgs scalars [12].

Our results are presented in Tabs. I–II and Figs. 2–8[10].

3.2 Top signals

As the techniques to measure the top parameters differ greatly depending on whether the collider is running around the $2m_t$ threshold or far above that, we will discuss separately the main features of processes (2)–(3) at the two CM energies considered.

$\sqrt{s} = 350$ GeV

Since one of the means of measuring m_t at an NLC is a threshold scan [19], Figs. 2a and 2b show the total cross sections in an interval around the top-antitop threshold at $2m_t$ for the case of $b\bar{b}W^\pm H^\mp$ and $b\bar{b}H^+H^-$ final states, respectively, for a selection of pseudoscalar Higgs masses (for larger values of M_A top decays into charged Higgs are well below detection level): in the case of the $e^+e^- \to t\bar{t}$ diagram alone as well as in presence of all graphs. Whereas in the case of two charged Higgses (see Fig.2b) the irreducible background is almost negligible (only a ten percent effect at the most can be noted very below threshold, at small M_A's), when only one of the top quarks decays into $bH^\pm$ pairs its effect can be drastically visible (see Fig. 2a). This is always true at small $\tan\beta$, whereas for large $\tan\beta$'s this is the case only at smaller values of M_A (for $M_A = 140$ GeV and $\tan\beta = 30$. the $t\bar{t}$ and the complete $b\bar{b}W^\pm H^\mp$ rates virtually coincide). To appreciate quantitatively the various effects entering in the curves of Fig. 2a–b we have displayed in three different columns (see Tabs. I and II) the cross sections due to: (i) the $e^+e^- \to t\bar{t}$ diagram in Narrow Width Approximation (NWA, $\Gamma \to 0$)[11]; (ii) the $e^+e^- \to t\bar{t}$ diagram with a finite width ($\Gamma = \Gamma_t$); (iii) all the diagrams (again with $\Gamma = \Gamma_t$) for both processes (2)–(3) and the two $\tan\beta$ values. This allows one to isolate the effect of the finite width Γ_t and of the irreducible background. We also report rates for three values of $M_{H^\pm}$ so that one can notice the heavy suppression of the total cross sections, which sets up as the charged Higgs mass increases and which

[10] Please note that, when reporting the rates corresponding to process (2) in the forthcoming Figures and Tables, we have considered only one of the two possible charge combinations of the $W^\pm$ and $H^\mp$ bosons. The cross sections for $e^+e^- \to b\bar{b}W^+H^-$ and $e^+e^- \to b\bar{b}H^+W^-$ are in fact identical because of charge conjugation. Therefore, the total production rates correspond to twice the values given in Tabs. I–II and Figs. 2–8. We have decided to do so in order to be able to plot in the same figures the spectra of both processes (2)–(3), the rates of the latter being generally smaller than those of the former.

[11] See Refs. [2, 5] for details.

is due to the decreasing branching ratio of the top into $bH^\pm$ pairs.

Thanks to our procedure of computing the 'total cross sections' (i.e., by summing different 'sub-cross sections' with a specific resonant structure) we have been able to identify which of the diagrams in Figs. 1a–b are responsible for the larger background contributions entering in Figs. 2a.

For example, for $\tan\beta = 1.5$, at $M_A = 60$ GeV, $h(A) \to bb$ resonant graphs (not including graph 12 in Fig. 1a) yield a contribution of $\approx 0.16(0.41)$ fb, at $\sqrt{s} = 340$ GeV. Of the two Higgs signals only $H^\pm \to hW^\pm \to b\bar{b}W^\pm$ is relevant, producing a rate of ≈ 8.68 fb, whereas $H^\pm \to tb \to b\bar{b}W^\pm$ is around 0.16 fb only ($M_{H^\pm} \approx 100$ GeV being a value well below the threshold at $m_t + m_b$). The single top resonant diagrams via $t \to bW^\pm$ (the square of diagram 6 plus its interference with graphs 2 and 9 in Fig. 1a) and via $t \to bH^\mp$ (the square of the sum of diagrams 1, 4 and 5 plus their interferences with graph 2 in Fig. 1a) produce the rates 0.10 and 0.46 fb, respectively. At the same point of CM energy the $t\bar{t}$ contribution is ≈ 2.47 fb. As $\sqrt{s}$ increases, the top-antitop signal clearly gets larger, eventually being the dominant part of the total rate: e.g., ≈ 72 fb at 360 GeV. The Higgs resonances h and A yield 0.19 and 0.52 fb at $\sqrt{s} = 360$ GeV, respectively, whereas the single-top ones produce 0.18 and 0.65 fb, in correspondence of $t \to bW^\pm$ and $t \to bH^\mp$ diagrams. The trend remains rather similar for $M_A = 100$ GeV (and $\tan\beta = 1.5$), whereas when $M_A = 140$ GeV (that is $M_{H^\pm} \approx 161$ GeV) phase space suppression effects become dominant. On the one hand, the off-shell $t\bar{t}$ production is well below detection level up to $\sqrt{s} \approx 346$ GeV. On the other hand, the $h(A) \to b\bar{b}$ resonant graphs are much smaller (their BRs remain constant but the sum $M_{h(A)} + M_{H^\pm} + M_{W^\pm}$ approaches(exceeds) the CM energy). Therefore, the bulk of the total cross section is due to the $H^\pm$ signals, $H^\pm \to hW^\pm \to b\bar{b}W^\pm$ being around 2.19 fb and $H^\pm \to tb \to b\bar{b}W^\pm$ approximately 3.45 fb (as $M_{H^\pm} \to m_t + m_b$), again at $\sqrt{s} = 340$ GeV. The phase space effect is very drastic on top decays, so that the difference between the $e^+e^- \to t\bar{t}$ curve and that produced by all the diagrams is largest in this case (i.e., $M_A = 140$ GeV). In fact, an increasing value of $M_{H^\pm}$ means a suppression of the BR$[t \to bH^\pm]$ and vice versa an enhancement of that for $H^\pm \to tb \to b\bar{b}W^\pm$ (also note that for $M_{H^\pm} \approx 161$ GeV one gets closer to a local maximum of the $H^\pm \to hW^\pm \to b\bar{b}W^\pm$ decay fraction [17]).

For $\tan\beta = 30.$ the two H^+H^- signals are generally negligible, because of the suppression coming from their BRs (see Ref. [17]), the dominant background effects being due to the $h \to b\bar{b}$ and $A \to b\bar{b}$ resonant graphs. At $\sqrt{s} = 340$ GeV and for $M_A = 60$ GeV, one gets that $H^\pm \to hW^\pm \to b\bar{b}W^\pm$ and $H^\pm \to tb \to b\bar{b}W^\pm$ are at the level of $\mathcal{O}(10^{-2})$ and $\mathcal{O}(10^{-4})$ fb, respectively, whereas the $h(A) \to b\bar{b}$ resonant graphs yield a contribution of 0.39(0.40) fb. However, as M_A increases the $h, A \to b\bar{b}$ resonances get smaller (they both are around 0.015 fb at $M_A = 100$ GeV and both completely negligible at $M_A = 140$ GeV, again for $\sqrt{s} = 340$ GeV). In fact, although the BRs for h and A bosons into $b\bar{b}$ pairs remain roughly constant for $M_A \lesssim 140$ GeV also for $\tan\beta = 30.$, it should be noticed that M_h grows with M_A more at large than at small $\tan\beta$'s. For example, at $M_A = 100(140)$ GeV and $\tan\beta = 30.$, one finds $M_h + M_{W^\pm} + M_{H^\pm} \approx 308(336)$ GeV. For such reasons then, the differences between $e^+e^- \to t\bar{t} \to b\bar{b}W^+W^-$ and $e^+e^- \to b\bar{b}W^+W^-$ rates are small for $M_A \gtrsim 100$ GeV and large $\tan\beta$'s.

A second technique of measuring m_t at threshold is the so-called end-point method in the spectrum of the boson produced in the top decay chain [19]. Whereas for events of the type $e^+e^- \to b\bar{b}W^+W^-$ this is necessarily a $W^\pm$ boson [2, 5], according to our detection strategy such a particle is in events of the type (2)–(3) a $H^\pm$ scalar, tagged in the $\tau\nu_\tau$ channel. In general, if one assumes an NWA for the top in $e^+e^- \to t\bar{t}$ (see eq. (1) in Ref. [2]), then the minimum and maximum values of p_H (and p_W) are fixed by the decay kinematics (see, e.g., [22]). This is clearly spoiled by a finite value of Γ_t (which introduces a Breit-Wigner dependence in the top propagator), whose effect consists in a smearing of the edges of the momentum distribution. The inclusion of all the other non-$t\bar{t}$ diagrams also mimic a similar effect. The p_H spectrum in presence of both finite top width and all graphs of Figs. 1a–b is given in the two upper windows of Figs. 3a–b (e.g., for $M_A = 60$ and 100 GeV). For reference, we also give the same distribution in the case of the $W^\pm$ boson (from $e^+e^- \to b\bar{b}W^\pm H^\mp$ events), spectrum which could well be plotted by means of the momentum of the jet-jet pair for which $M_{\rm jj} \approx M_{W^\pm}$. From their comparison with the curves in NWA (lower windows) one can easily deduce the difficulty in recognising any end-point in the distributions when all effects are properly included, those more visible (the long tails at large momentum for $e^+e^- \to b\bar{b}W^\pm H^\mp$) being clearly due to the irreducible background. It is also interesting to notice the single bin filled on the right hand side of the two upper plots in Fig. 3a, for the case of the p_H spectrum in reaction (2). This is due to the $e^+e^- \to H^+H^-$ diagrams (graphs 9 and 12 in Fig. 1a), for which the momentum of the $H^\pm$'s is fixed via the relation $p_H = \sqrt{s/4 - M^2_{H^\pm}}$. The rate of this bin is regulated by the interplay between the cross section for $e^+e^- \to H^+H^-$ and the charged Higgs BRs into $hW^\pm$ and tb pairs, so that the bin practically disappears for $\tan\beta = 30.$, for which the latter are both heavily suppressed (when $M_A \lesssim 100$ GeV).

$\sqrt{s} = 500$ GeV

Far above the $2m_t$ threshold (in our case, $\sqrt{s} = 500$ GeV) one can determine the top mass from the two three-jet invariant mass distributions that can be reconstructed from the $b\bar{b}{\rm jj}\tau\nu_\tau$ final state [19]. In fact, in $b\bar{b}W^\pm H^\mp$ and $b\bar{b}H^+H^-$ events in which one final state boson decays hadronically (let us say the positive charged one B^+, where $B^\pm = W^\pm, H^\pm$) and the other leptonically, there are two possible three-jet combinations among the jj pair reconstructing the boson mass (i.e., those for which $M_{\rm jj} \approx M_{W(H)^\pm}$) and the two b's: the 'right' one (B^+b), peaking at m_t, and the 'wrong' one ($B^+\bar{b}$), producing a rather broad and flat spectrum (we assume that the charge of the b-jets is not recognised). They are both plotted in Figs. 4a and b, for both reactions (2)–(3). For comparison, in case of $b\bar{b}W^\pm H^\mp$ events we also give the similar distribution which can be obtained by combining the tagged $H^\pm$ with the two bottom quarks. Note that by 'b-quarks' we mean here the two jets that do not peak at $M_{W(H)^\pm}$[12]. Note the logarithmic scale of the figures, as well as the rather thin binning (2 GeV) of the distributions. In other terms, although in this case the 'wrong' distributions are well below the 'right' ones, it must be remembered that for resolutions worse than that considered here the peaks would be cut down, whereas the flat spectra would remain the same. Therefore, the possibility of clearly identifying the top resonance drastically

[12]The tagging procedure can be simplified if μ-vertex tagging techniques are exploited on the two b-quarks, so that the requirement $M_{\rm jj} \approx M_{W(H)^\pm}$ needs not to be applied.

depends on the angle and energy resolution of each single jet.

For reference, the cross sections at $\sqrt{s} = 500$ GeV for process (2) are (no charge conjugation included): 105(114) fb for $\tan\beta = 1.5$ and 61(64) fb for $\tan\beta = 30.$ when $M_A = 60$ GeV; 61(76) fb for $\tan\beta = 1.5$ and 35(37) fb for $\tan\beta = 30.$ when $M_A = 100$ GeV. At the same energy, in case of reaction (3) one obtains: 24(24) fb for $\tan\beta = 1.5$ and 8.5(8.6) fb for $\tan\beta = 30.$ when $M_A = 60$ GeV; 6.4(6.5) fb for $\tan\beta = 1.5$ and 2.3(2.4) fb for $\tan\beta = 30.$ when $M_A = 100$ GeV. The numbers in brackets refer to the rates obtained when all diagrams are calculated whereas the others to the case of top-antitop production and decay only (in both cases $\Gamma = \Gamma_t$). From these numbers, one realises that in case of $e^+e^- \to b\bar{b}H^+H^-$ events the effects of the irreducible background are negligible, whereas for the process $e^+e^- \to b\bar{b}W^\pm H^\mp$ they can amount to several percent (also at $\sqrt{s} = 500$ GeV).

3.3 Higgs signals

Let us now turn to the case of Higgs resonances. We have chosen only a few representative cases, where Higgs peaks can be visible in the decay spectra and show peculiar features. First of all, it is instructive to plot the invariant mass of the $b\bar{b}$ system, when all diagrams are computed. This is done in Fig. 5a for the combination $M_A = 60$ GeV and $\tan\beta = 1.5$, at $\sqrt{s} = 350$ GeV, for both processes (2)–(3), and in Fig. 5b for the case $M_A = 140$ GeV and $\tan\beta = 1.5$, at $\sqrt{s} = 500$ GeV, for reaction (2) only. If the resolution in invariant mass of the $b\bar{b}$ system is 5 GeV, at lower energy only the spectrum from process (2) shows a resonance (see Fig. 5a, continuous histogram in the main plot). However, this peak actually hides a superposition of two $M_{b\bar{b}}$ resonances, due to decaying h and A bosons (in order of increasing mass), as it can be appreciated in the central insert, where a binning of 1 GeV is used. If such higher resolution can be achieved, one can possibly disentangle the $h \to b\bar{b}$ peak from reaction (3) (lower-right insert) whereas the $H \to b\bar{b}$ one from process (2) remains overwhelmed by the background (its position is located by the arrow in the upper-right insert). At larger energies, phase space effects do not suppress any longer the production of the heaviest neutral Higgs scalar. In fact, at $\sqrt{s} = 500$ GeV, for $M_A = 140$ GeV and $\tan\beta = 1.5$, the resonances of all three neutral Higgses of the $\mathcal{MSSM}$ can be recognised (see Fig. 5b). In general, note that, although such plots might be somewhat superfluous if one wants to optimise the cuts in order to enhance $e^+e^- \to t\bar{t}$ and reduce the background (in fact, by the time of the advent of an NLC the values of M_{Higgs} might already be known), in contrast their knowledge will be essential if one would like to attempt studies of the gauge structure of the $\mathcal{MSSM}$, as mentioned in footnote 6. Like for the case of top signals, we again treat the case of charged Higgs signals at $\sqrt{s} = 350$ and 500 GeV separately.

$\sqrt{s} = 500$ GeV

We continue this Subsection by discussing the potential of a $\sqrt{s} = 500$ GeV NLC in detecting charged Higgses produced in $e^+e^- \to H^+H^-$ scatterings, in which one of the scalars decays into $hW^\pm \to b\bar{b}W^\pm$ and/or $tb \to b\bar{b}W^\pm$. In Figs. 6a–b we display the differential distributions in the invariant mass of the system $b\bar{b}W^\pm$ (i.e., the hadronic four-jet subset, as $W^\pm \to$ jj), at $\sqrt{s} = 500$ GeV and for $M_A = 140, 180$ and 220 GeV (both values of $\tan\beta$ are considered). For all pseudoscalar Higgs masses we give the results as produced by the full set of Feynman diagrams, whereas in the case $M_A = 140$ GeV we also plot the two resonant $H^\pm$ contributions separately (upper two windows). Note that, on the one hand, we consider A masses larger than 140 GeV (i.e., $M_{H^\pm} \gtrsim 161$ GeV) to allow for large values of the two Higgs BRs into $hW^\pm$ and tb (either or both), on the other hand, we restrict ourself to the case $M_A \lesssim 220$ GeV because of the maximum CM energy available. It is interesting to notice how the spectra produced by the non-H^+H^- diagrams steeply increase at $M_{b\bar{b}W^\pm} \approx 170 - 180$ GeV (roughly, the top rest mass: compare the lower window in Fig. 6a against the two upper ones). This is somewhat fortunate, as for $M_A = 140$ GeV the charged Higgs peak lies right a few GeV below that. Furthermore, for this value of M_A and for $\tan\beta = 1.5$, the Higgs production and decay rates are similar in the two channels (compare the continuous curves in the two upper frames of Fig. 6a). This could allow one (after implementing an appropriate selection requirement: e.g., $M_{b\bar{b}} \approx M_h$) to separate the hW decay from the tb one. In fact, for larger values of $M_{H^\pm}$ the Higgs signals come in practise from top-bottom decays only (see Fig. 6b). For $\tan\beta = 30.$ this is also true at $M_A \approx 140$ GeV [17], as it can be appreciated by comparing the dashed curves in the two upper sections of Fig. 6a.

Since the rates given in Figs. 6a–b do not include the BR into $\tau\nu_\tau$ pairs of one of the $H^\pm$ bosons and since this becomes very small for $M_A \gtrsim 140$ GeV at small $\tan\beta$'s [17], one has to face the following scenario (assuming the nominal integrated luminosity $\int \mathcal{L}dt = 10$ fb^{-1}). If $\tan\beta$ is large, charged Higgs signals can be produced at large rate at an NLC with $\sqrt{s} = 500$ GeV and certainly detected in the $H \to tb \to b\bar{b}W^\pm$ channel for $M_{H^\pm} \gtrsim 161$ GeV. In contrast, for small $\tan\beta$'s, this is true only for $M_A \approx 140 - 150$ GeV, region where the 'narrow' contribution from the hW channel compensates the small below threshold branching ratio into tb pairs.

$\sqrt{s} = 350$ GeV

Concerning smaller values of CM energy, that is $\sqrt{s} = 350$ GeV, it must be said that phase space suppression largely counterbalances the increase of the production cross section due to the s-channel dynamics of $e^+e^- \to H^+H^-$ events. In the very end the spectrum of charged Higgs masses which can be covered by the two mentioned decay channels at that energy is rather narrow, about 20 GeV, and only if $\tan\beta = 1.5$. In fact, for such a value, when $M_{H^\pm}$ is below 130 GeV or so, the total BR into the two Higgs channels is smaller than 0.1%. When instead $M_{H^\pm} \gtrsim 150$ GeV the production cross section fall below detection level [12]. If $\tan\beta = 30.$ such a window disappears completely. For these reason then, we decided not to focus our attention on the threshold energy stage of the NLC, in the case of charged Higgs searches via $e^+e^- \to H^+H^-$.

3.4 Mass dependence

So far, we have concentrated in our analysis on the case of selected values of M_A (or, equivalently, of $M_{H^\pm}$). However, as the effects due to the finite widths and to the irreducible backgrounds are equally present over all the available charged Higgs mass range, in this closing Subsection we intend to generalise our results by presenting various rates for processes (2)–(3) as a function of $M_{H^\pm}$ (again, at fixed $\tan\beta = 1.5$ and 30.). We do so, e.g., at the CM energy value of $\sqrt{s} = 500$ GeV, as we have noticed that a second stage NLC allows one to study contemporaneously both $e^+e^- \to t\bar{t}$ and $e^+e^- \to H^+H^-$ events.

Fig. 7 shows the cross sections for the same three processes as defined in Tab. I–II, for both reactions (2)–(3), but now at $\sqrt{s} = 500$ GeV and over the continuous mass range 60 GeV $\lesssim M_A \lesssim 240$ GeV (i.e., 100 GeV $\lesssim M_{H^\pm} \lesssim 252$ GeV). A comparison between the rates obtained in NWA (i.e., continuous lines) and those from the production and decay diagram only (i.e., dashed lines) illustrates that finite width effects clearly becomes larger as the difference $\Delta M = m_t - M_{H^\pm} - m_b$ gets smaller, the latter being positive. If negative, the rates of the NWA are identically zero. For $M_{H^\pm}$ well below m_t the effects are negligible (also compare to Figs. 2a–b at $\sqrt{s} = 350$ GeV). Furthermore, as the top width does not vary drastically, from approximately 1.72(1.78) GeV at $M_A = 60$ GeV and $\tan\beta = 1.5(30.)$ down to around 1.40 GeV at $M_A = 150$ GeV, where only the $\mathcal{SM}$ decay channel $t \to bW^\pm$ survives (see Fig. 2b of Ref. [5]), width effects are (above the $t \to bH^\pm$ threshold) rather independent from $M_{H^\pm}$. The total rate of process (2) is, in comparison to that of $e^+e^- \to t\bar{t} \to b\bar{b}W^\pm H^\mp$ events, much larger than the cross section of reaction (3) is with respect to the corresponding $e^+e^- \to t\bar{t} \to b\bar{b}H^+H^-$ rates. As already outlined in Section 3.1, this is due to the much richer variety of non-$t\bar{t}$ events that are active in the first case (especially the charged Higgs resonances: notice, e.g., the onset of the top-bottom channel at large $M_{H^\pm}$'s and $\tan\beta = 30.$).

In Fig. 8 we have plotted the cross sections of the two possible Higgs mechanisms entering in $e^+e^- \to b\bar{b}W^\pm H^\mp$ events: i.e., via $H^\pm \to tb$ and $H^\pm \to hW^\pm$ decays (actually, the second channel is only considered at small $\tan\beta$'s, because of the vanishing BR at larger values [17]). For both channels, the figure shows rates as obtained by multiplying the total $e^+e^- \to H^+H^-$ production rates times the branching ratios BR($H^\pm \to tb$) and BR($H^\pm \to hW^\pm$) (i.e., assuming on-shell production and neglecting the Higgs widths) and those produced by the subamplitudes involving the two mentioned resonances in our ME, along with the yield of all $e^+e^- \to b\bar{b}W^\pm H^\mp$ diagrams. Whereas the effects of the finite width of the $H^\pm$-bosons are generally small in both Higgs channels (possibly apart from the $H^\pm \to hW^\pm$ channel for $M_{H^\pm} \approx m_t$ at $\tan\beta = 1.5$), the irreducible background is overwhelming the signals up to $M_{H^\pm} \approx 150$ GeV (that is, as long as the $t \to bH^\pm$ channel is well open), the rates of the two remaining comparable up to charged Higgs masses around 200 GeV. Above $M_{H^\pm} \approx 150$ GeV, it is the $H^\pm \to tb$ component of the $e^+e^- \to b\bar{b}W^\pm H^\mp$ cross sections which accounts for the total rate, this being modulated at large values of $M_{H^\pm}$ by a phase space suppression. Since the largest part of the cross section of non-Higgs diagrams in $e^+e^- \to b\bar{b}W^\pm H^\mp$ events is due to $t\bar{t}$ events, the implementation of a cut like $M_{jjj} \neq m_t$ (on the three-jet invariant mass distributions that can be reconstructed from the $b\bar{b}jj\tau\nu_\tau$ signature) should allow one to largely increase the Higgs signal-to-background ratio. However, notice that in Section 3.3 no such cut was enforced, the Higgs peaks still being visible in many instances. This makes clear that concrete chances of Higgs detection exist for charged scalars of the $\mathcal{MSSM}$ produced via $e^+e^- \to H^+H^-$ interactions and decaying via either $H^\pm \to hW^\pm$ or $H^\pm \to tb$ at $\sqrt{s} = 500$ GeV e^+e^- Linear Colliders.

4. Summary and conclusions

In this paper we have studied the processes

$$e^+e^- \to b\bar{b}W^\pm H^\mp \qquad \text{and} \qquad e^+e^- \to b\bar{b}H^+H^-,$$

by computing their complete matrix elements at tree-level and integrating these over the corresponding phase spaces to produce total and differential cross sections relevant to phenomenological studies at the NLC. We focused our attention on the CM energies of $\sqrt{s} = 350$ GeV (top-antitop threshold, first stage NLC) and 500 GeV (final stage NLC).

These processes are experimentally interesting since they both include among the various contributions the production of top-antitop pairs eventually decaying via the channels $t \to bW^\pm$ and $t \to bH^\pm$. Furthermore, in the case of $b\bar{b}W^\pm H^\mp$ final states one can also study the charged Higgs production process $e^+e^- \to H^+H^-$ followed by the decay of one of the $H^\pm$'s via hW and/or tb pairs, with $h \to b\bar{b}$ and $t \to bW$.

Numerical analyses have been carried out in order to quantify, first, the influence of finite top width and irreducible background effects on the integrated and differential rates as obtained from $e^+e^- \to t\bar{t}$ events in NWA and, second, to establish the detectability of the mentioned Higgs processes, as a function of the values assumed by the fundamental parameters of the $\mathcal{MSSM}$.

For certain combinations of M_A and $\tan\beta$, our results indicate that, on the one hand, finite width and background effects must be included in the simulations aiming to measure precisely the top parameters and, on the other hand, charged Higgs signal in the mass range 140 GeV $\lesssim M_{H^\pm} \lesssim \sqrt{s}/2$ can be promptly detected at nominal luminosity, especially if $\sqrt{s}$ and $\tan\beta$ are large.

The numerical codes we have used in our analysis can be easily folded with the experimental Monte Carlo simulation programs (including beam and detector effects) used by the NLC Working Groups, in order to quantify correctly irreducible background effects in top studies as well as to optimise the selection strategy of charged Higgs signals. In this respect, note that we have always assumed one of the two bosons in the final state to decay into $\tau\nu_\tau$ pairs, which is clearly restrictive in the case of Higgs searches for large values of M_A and small $\tan\beta$'s. Indeed, dedicated experimental simulations might well assess that other H^+H^- decay signatures are also relevant, so that we make our matrix elements available to the public for further studies.

Finally, we also have pointed out the importance of events of the type discussed here in order to study the gauge structure of the Higgs sector of the $\mathcal{MSSM}$, as they involve many of the tree-level Higgs vertices of the theory.

5. Acknowledgements

SM is grateful to the UK PPARC and KO to Trinity College and the Committee of Vice-Chancellors and Principals of the Universities of the United Kingdom for financial support. This work is sponsored in part by the EC Programme "Human Capital and Mobility", Network "Physics at High Energy Colliders", contract CHRX-CT93-0357 (DG 12 COMA).

References

[1] Proceedings of the Workshop "e^+e^- *Collisions at 500 GeV. The Physics Potential* ", Munich, Annecy, Hamburg, 3–4 February 1991, ed. P.M. Zerwas, DESY 92–123A/B, August 1992, DESY 93–123C, December 1993.

[2] A. Ballestrero, E. Maina and S. Moretti, *Phys. Lett.* **B333** (1994) 434.

[3] A. Ballestrero, E. Maina and S. Moretti, *Phys. Lett.* **B335** (1994) 460.

[4] A. Ballestrero, V.A. Khoze, E. Maina, S. Moretti and W.J. Stirling, *Z. Phys.* **C72** (1996) 71.

[5] S. Moretti, *Z. Phys.* **C73** (1997) 653.

[6] S. Moretti, *preprint* Cavendish-HEP-96/17, October 1996 (to be published in *Z. Phys.* **C**).

[7] Proceedings of the Workshop on "*Physics at Current Accelerators and Supercolliders* ", eds. J. Hewett, A. White and D. Zeppenfeld, Argonne National Laboratory, 1993.

[8] G. Altarelli, T. Sjöstrand and F. Zwirner, eds., '*Report of the Workshop on Physics at LEP2*', CERN 96–01 (1996).

[9] CMS Technical Proposal, CERN/LHC/94-43 LHCC/P1, December 1994.

[10] ATLAS Technical Proposal, CERN/LHC/94-43 LHCC/P2, December 1994.

[11] Proceedings of the Workshop on "*High Luminosities at LEP* ", CERN Report 91-02, Geneva, Switzerland.

[12] See, e.g.:
A. Djouadi, J. Kalinowski and P.M. Zerwas, in Ref. [1], part A (and references therein);
P. Eerola and J. Sirkka, in Ref. [1], part A (and references therein);
A. Djouadi, H.E. Haber, P. Igo-Kemenes, P. Janot and P.M. Zerwas (conveners), 'Higgs Particles', in Proceedings of the Workshop "*Physics with* e^+e^- *Colliders*", Annecy, Gran Sasso, Hamburg, 4 February – 1 September 1995, ed. P.M. Zerwas, KA-TP-16-96, May 1996.

[13] K. Hagiwara and D. Zeppenfeld, *Nucl. Phys.* **B274** (1986) 1.

[14] H. Murayama, I. Watanabe and K. Hagiwara, HELAS: HELicity Amplitude Subroutines for Feynman Diagram Evaluations, *KEK Report* 91-11, January 1992.

[15] G.P. Lepage, *Jour. Comp. Phys.* **27** (1978) 192.

[16] P. Grannis, presented at the ICHEP96 Conference, Warsaw (1996).

[17] S. Moretti and W.J. Stirling, *Phys. Lett.* **B347** (1995) 291; Erratum, *ibidem* **B366** (1996) 451.

[18] J. Guasch and J. Solà, *preprint* UAB-FT-389, March 1996.

[19] G. Bagliesi *et al.*, in Ref. [1], part A.

[20] A. Blondel, plenary talk presented at ICHEP96, Warsaw, Poland, 25-31 July 1996, to appear in the proceedings.

[21] A. Djouadi, J. Kalinowski and P.M. Zerwas, in Ref. [1], part A (and references therein).

[22] E. Byckling and K. Kajantie, 'Particle kinematics', Wiley, London 1973.

[23] T. Stelzer and W.F. Long, *Comp. Phys. Comm.* **81** (1994) 357.

Table Captions

Tab. I Cross sections in femtobarns for $e^+e^- \to t\bar{t}$ (NWA, $\Gamma \to 0$), for $e^+e^- \to t\bar{t} \to b\bar{b}W^\pm H^\mp$ (production and decay diagram only, $\Gamma = \Gamma_t$) and for $e^+e^- \to b\bar{b}W^\pm H^\mp$ (all diagrams at tree-level, $\Gamma = \Gamma_t$), at $\sqrt{s} = 350$ GeV, for $m_t = 174$ GeV, and $M_A = 60(140)[220]$ GeV (i.e., $M_{H^\pm} \approx 100(161)[234]$). The first(second) row reports rates for $\tan\beta = 1.5(30.)$.

Tab. II Cross sections in femtobarns for $e^+e^- \to t\bar{t}$ (NWA, $\Gamma \to 0$), for $e^+e^- \to t\bar{t} \to b\bar{b}H^+H^-$ (production and decay diagram only, $\Gamma = \Gamma_t$) and for $e^+e^- \to b\bar{b}H^+H^-$ (all diagrams at tree-level, $\Gamma = \Gamma_t$), at $\sqrt{s} = 350$ GeV, for $m_t = 174$ GeV, and $M_A = 60(140)[220]$ GeV (i.e., $M_{H^\pm} \approx 100(161)[234]$). The first(second) row reports rates for $\tan\beta = 1.5(30.)$.

Figure Captions

Fig. 1 The $\mathcal{MSSM}$ Feynman topologies contributing at lowest order to process (2) (**a**) and (3) (**b**). The label 'h(h')' represents any of the neutral Higgses of the theory, H, h and A, whereas 'H' refers to the charged scalar, $H^\pm$. 'A', 'Z' and 'W' represent the gauge bosons γ, Z and $W^\pm$. Note that for process (2) we plot the diagrams for the charge combination W^-H^+ only, those corresponding to the case W^+H^- being trivially deducible from the one given here. The figure has been produced with the help of the package MadGraph [23]. For reference, in (**c**) we present the branching ratios of t-quarks and $H^\pm$-bosons as functions of the charged Higgs mass in the range 60 GeV $\lesssim M_{H^\pm} \lesssim$ 240 GeV, for $\tan\beta = 1.5$ and 30.

Fig. 2 Cross section in femtobarns for $e^+e^- \to b\bar{b}W^\pm H^\mp$ (**a**) and $e^+e^- \to b\bar{b}H^+H^-$ (**b**) events around the top-antitop threshold, for three different values of M_A. Continuous lines: $\tan\beta = 1.5$ and production and decay diagram only. Dashed lines: $\tan\beta = 1.5$ and all diagrams. Dotted lines: $\tan\beta = 30.$ and production and decay diagram only. Dash-dotted lines: $\tan\beta = 30.$ and all diagrams. In all cases $\Gamma = \Gamma_t$ has been used. Note the superposition of curves in some instances.

Fig. 3 Differential distributions in the momentum of the $W^\pm$ and $H^\pm$ bosons, in $e^+e^- \to b\bar{b}W^\pm H^\mp$ and $e^+e^- \to b\bar{b}H^+H^-$ events, for two values of M_A, with $\tan\beta = 1.5$ (**a**) and 30. (**b**). The two following cases are considered: NWA (lower windows) and all diagrams (upper windows). The CM energy is $\sqrt{s} = 350$ GeV. Continuous lines: $W^\pm$ momentum in $e^+e^- \to b\bar{b}W^\pm H^\mp$ events. Dashed lines: $H^\pm$ momentum in $e^+e^- \to b\bar{b}W^\pm H^\mp$ events. Dotted lines: $H^\pm$ momentum in $e^+e^- \to b\bar{b}H^+H^-$ events.

Fig. 4 Differential distributions in the invariant mass of the 'right' and 'wrong' three-jet combinations (see the text), in $e^+e^- \to b\bar{b}W^\pm H^\mp$ and $e^+e^- \to b\bar{b}H^+H^-$ events, for $M_A = 60$ (upper window) and 100 (lower window) GeV, with $\tan\beta = 1.5$ (**a**) and 30. (**b**). All diagrams have been here considered. The CM energy is $\sqrt{s} = 500$ GeV. Continuous lines: $M_{bW^\pm}$ mass in $e^+e^- \to b\bar{b}W^\pm H^\mp$ events. Dashed lines: $M_{bH^\pm}$ mass in $e^+e^- \to b\bar{b}W^\pm H^\mp$ events. Dotted lines: $M_{bH^\pm}$ mass in $e^+e^- \to b\bar{b}H^+H^-$ events.

Fig. 5 Differential distributions in invariant mass of the $b\bar{b}$ pair. (**a**) In $e^+e^- \to b\bar{b}W^\pm H^\mp$ and $e^+e^- \to b\bar{b}H^+H^-$ events, for $\tan\beta = 1.5$ GeV, $M_A = 60$ GeV and $\sqrt{s} = 350$ GeV. Continuous lines (main window): all $e^+e^- \to b\bar{b}W^\pm H^\mp$ diagrams. Dashed lines (main window): all $e^+e^- \to b\bar{b}H^+H^-$ diagrams. The two small windows on the right show the regions around the H (in $e^+e^- \to b\bar{b}W^\pm H^\mp$, upper one) and h (in $e^+e^- \to b\bar{b}H^+H^-$, lower one) resonances enlarged and plotted with high resolution, together with the $t\bar{t}$ contribution ($\Gamma = \Gamma_t$, shaded). The small central window does the same for the h and A 'resolved' resonances in the case of $e^+e^- \to b\bar{b}W^\pm H^\mp$ events. (**b**) In $e^+e^- \to b\bar{b}W^\pm H^\mp$ events, for $\tan\beta = 1.5$ GeV, $M_A = 140$ GeV and $\sqrt{s} = 500$ GeV. Dashed line: all diagrams. Continuous line: $t\bar{t}$ contribution ($\Gamma = \Gamma_t$, shaded).

Fig. 6 Differential distributions in invariant mass of the $b\bar{b}W^{\pm}$ system, in $e^+e^- \to b\bar{b}W^{\pm}H^{\mp}$ events, for $\tan\beta = 1.5$ and 30., $M_A = 140$ (**a**) and 180, 220 GeV (**b**), at $\sqrt{s} = 500$ GeV. In the case $M_A = 140$ GeV the resonant $H^{\pm} \to hW^{\pm}$ (upper plot) and $H^{\pm} \to tb$ (middle plot) contributions are shown separately. Continuous lines: $\tan\beta = 1.5$. Dashed lines: $\tan\beta = 30$.

Fig. 7 Cross section in femtobarns for $e^+e^- \to b\bar{b}W^{\pm}H^{\mp}$ (upper three curves) and $e^+e^- \to b\bar{b}H^+H^-$ (lower three curves) events at $\sqrt{s} = 500$ GeV as a function of $M_{H^{\pm}}$, for $\tan\beta = 1.5$ (upper plot) and $\tan\beta = 30.$ (lower plot). Continuous lines: $e^+e^- \to t\bar{t}$ (NWA, $\Gamma \to 0$). Dashed lines: $e^+e^- \to t\bar{t} \to b\bar{b}W^{\pm}H^{\mp}$ and $e^+e^- \to t\bar{t} \to b\bar{b}H^+H^-$ (production and decay diagrams only, $\Gamma = \Gamma_t$). Dotted lines: $e^+e^- \to b\bar{b}W^{\pm}H^{\mp}$ and $e^+e^- \to b\bar{b}H^+H^-$ (all diagrams at tree-level, $\Gamma = \Gamma_t$).

Fig. 8 Cross section in femtobarns for $e^+e^- \to b\bar{b}W^{\pm}H^{\mp}$ events at $\sqrt{s} = 500$ GeV as a function of $M_{H^{\pm}}$, for $\tan\beta = 1.5$ (upper plot) and $\tan\beta = 30.$ (lower plot). Continuous lines: $\sigma(e^+e^- \to H^+H^-) \times \mathrm{BR}(H^{\pm} \to tb \to b\bar{b}W^{\pm})$. Dashed lines: $e^+e^- \to H^+H^- \to tbH^{\mp} \to b\bar{b}W^{\pm}H^{\mp}$. Dotted lines: $\sigma(e^+e^- \to H^+H^-) \times \mathrm{BR}(H^{\pm} \to hW^{\pm} \to b\bar{b}W^{\pm})$. Double-dash lines: $e^+e^- \to H^+H^- \to hW^{\pm}H^{\mp} \to b\bar{b}W^{\pm}H^{\mp}$. Dash-dotted lines: $e^+e^- \to b\bar{b}W^{\pm}H^{\mp}$ (all diagrams at tree-level, $\Gamma = \Gamma_t$).

m_t (GeV)	$\sigma(e^+e^- \rightarrow X)$ (fb)		
	$t\bar{t}$	$t\bar{t} \rightarrow \bar{b}bW^{\pm}H^{\mp}$	$\bar{b}bW^{\pm}H^{\mp}$
174	$34.64(2.21)[1.32 \times 10^{-18}]$	$30.55(1.73)[2.57 \times 10^{-8}]$	$40.50(10.32)[9.48 \times 10^{-8}]$
	$20.04(1.30)[6.37 \times 10^{-19}]$	$17.57(1.01)[1.24 \times 10^{-8}]$	$18.89(1.05)[9.33 \times 10^{-8}]$
$\sqrt{s} = 350$ GeV			

Tab. I

m_t (GeV)	$\sigma(e^+e^- \rightarrow X)$ (fb)		
	$t\bar{t}$	$t\bar{t} \rightarrow \bar{b}bH^+H^-$	$\bar{b}bH^+H^-$
174	$7.87(2.17 \times 10^{-2})[0.00]$	$6.98(1.46 \times 10^{-2})[0.00]$	$7.10(1.46 \times 10^{-2})[0.00]$
	$2.84(7.50 \times 10^{-3})[0.00]$	$2.49(5.04 \times 10^{-3})[0.00]$	$2.52(5.05 \times 10^{-3})[0.00]$
$\sqrt{s} = 350$ GeV			

Tab. II

Diagrams by MadGraph

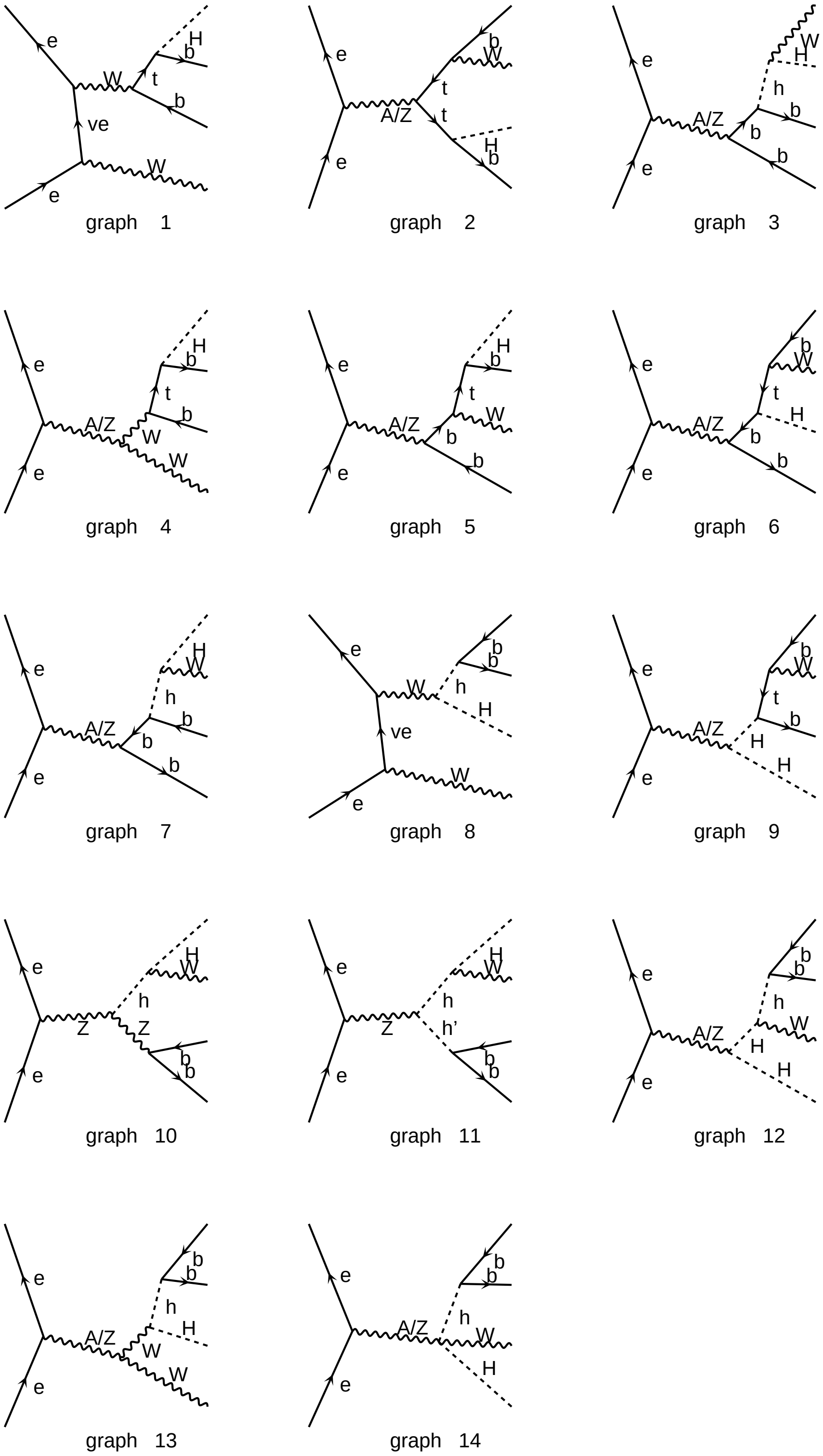

Fig. 1a

Diagrams by MadGraph

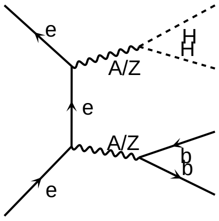

graph 1

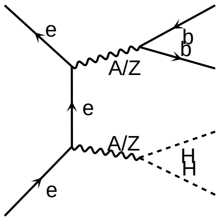

graph 2

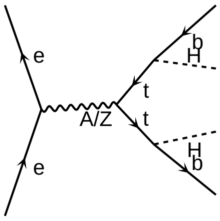

graph 3

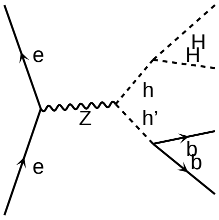

graph 4

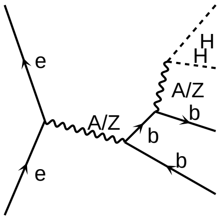

graph 5

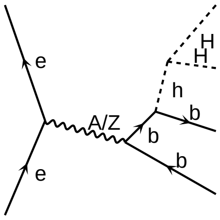

graph 6

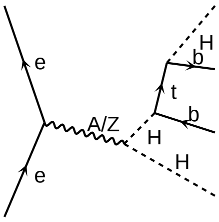

graph 7

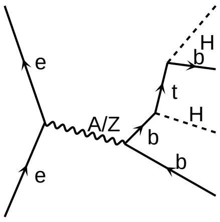

graph 8

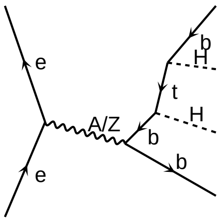

graph 9

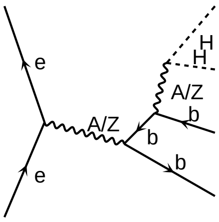

graph 10

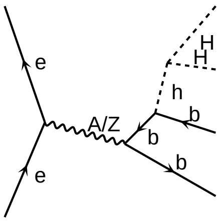

graph 11

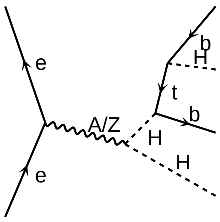

graph 12

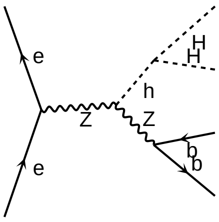

graph 13

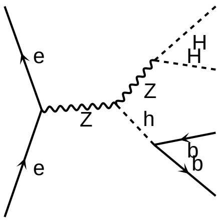

graph 14

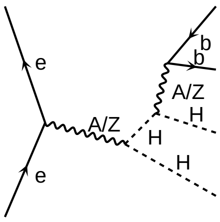

graph 15

continues

Diagrams by MadGraph

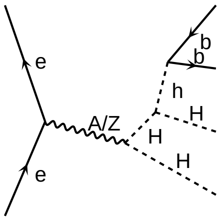

graph 16

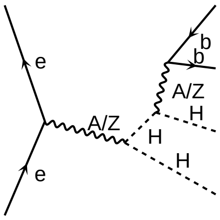

graph 17

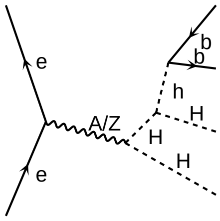

graph 18

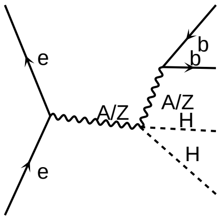

graph 19

Fig. 1b

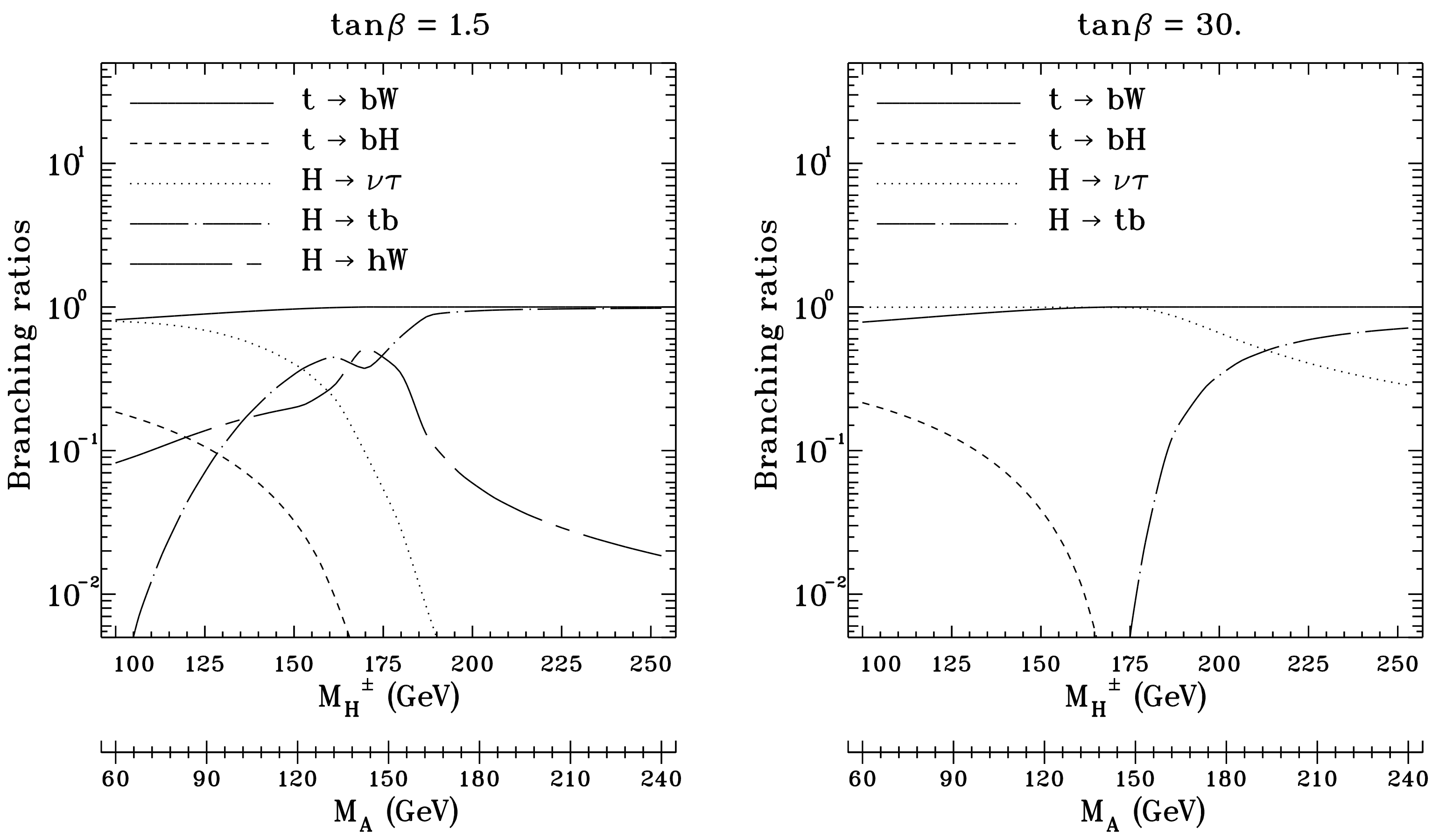
tanβ = 1.5
t → bW
t → bH
H → ντ
H → tb
H → hW
Branching ratios
10^1
10^0
10^-1
10^-2
100 125 150 175 200 225 250
M_H± (GeV)
60 90 120 150 180 210 240
M_A (GeV)
tanβ = 30.
t → bW
t → bH
H → ντ
H → tb
Branching ratios
10^1
10^0
10^-1
10^-2
100 125 150 175 200 225 250
M_H± (GeV)
60 90 120 150 180 210 240
M_A (GeV)

Fig. 1c

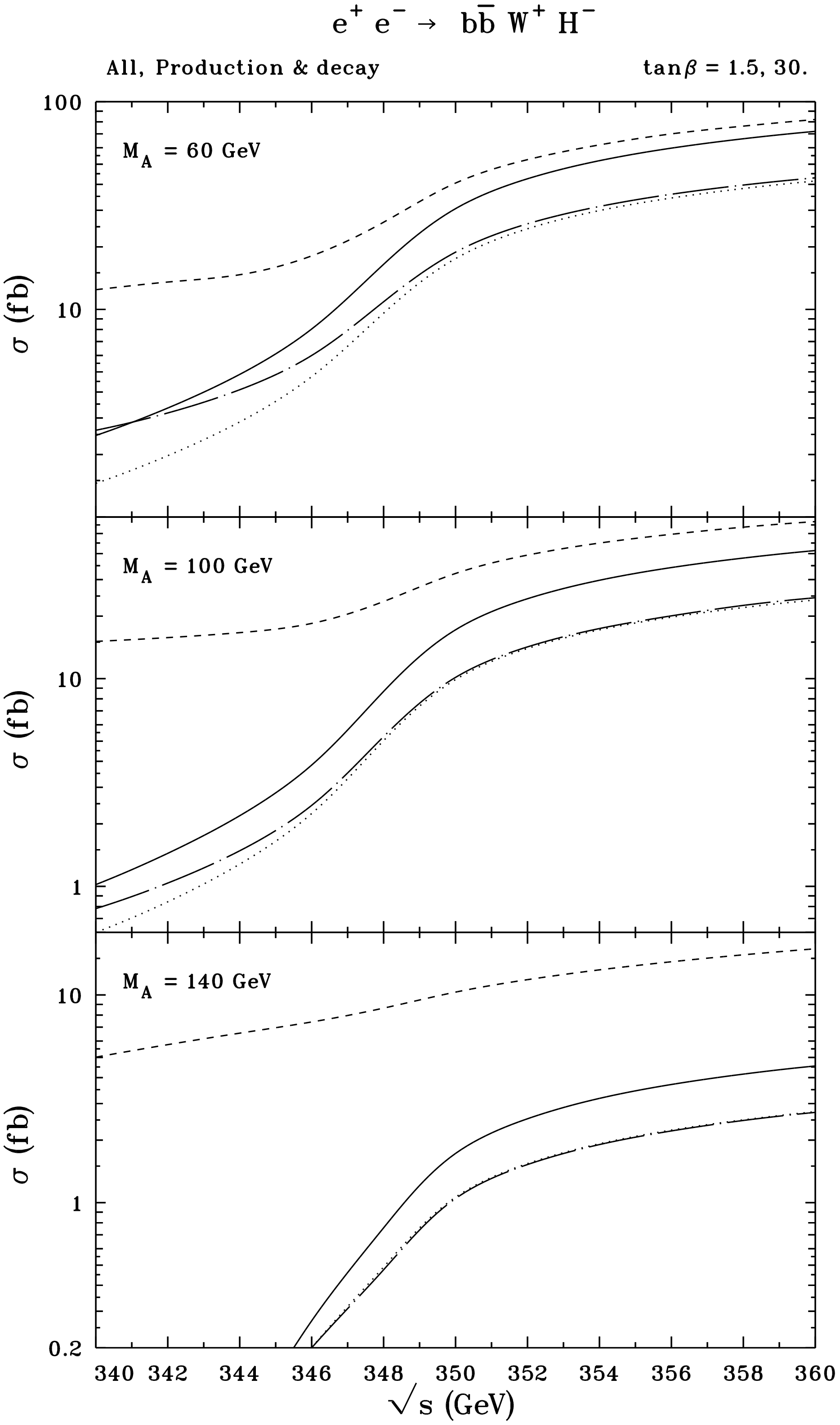

$e^+ e^- \to b\bar{b} W^+ H^-$
All, Production & decay
$\tan\beta$ = 1.5, 30.
M_A = 60 GeV
M_A = 100 GeV
M_A = 140 GeV
σ (fb)
100
10
1
0.2
340
342
344
346
348
350
352
354
356
358
360
$\sqrt{s}$ (GeV)

Fig. 2a

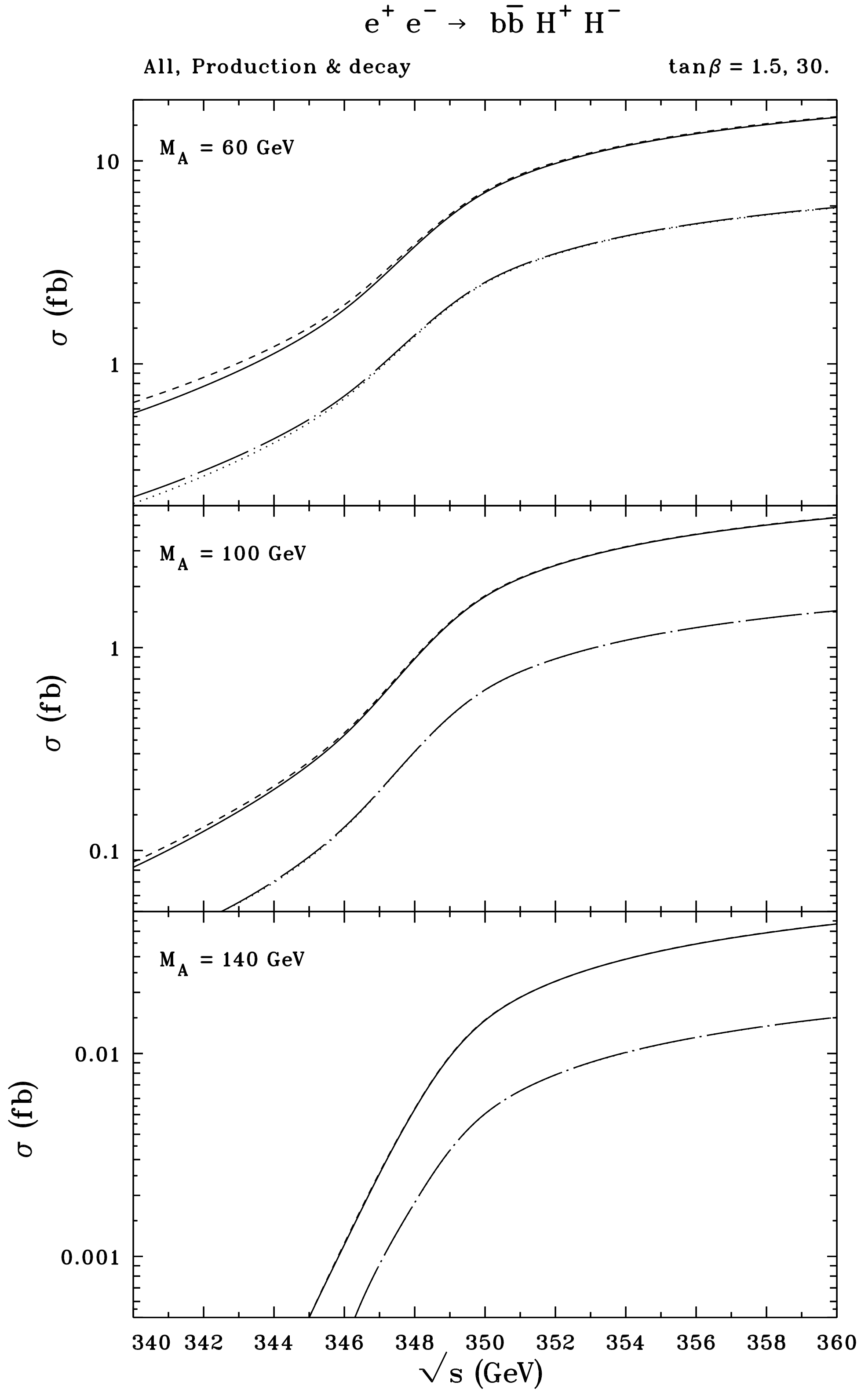

$e^+ e^- \to b\bar{b} H^+ H^-$
All, Production & decay
$\tan\beta$ = 1.5, 30.
M_A = 60 GeV
M_A = 100 GeV
M_A = 140 GeV
10
1
0.1
0.01
0.001
σ (fb)
340 342 344 346 348 350 352 354 356 358 360
$\sqrt{s}$ (GeV)

Fig. 2b

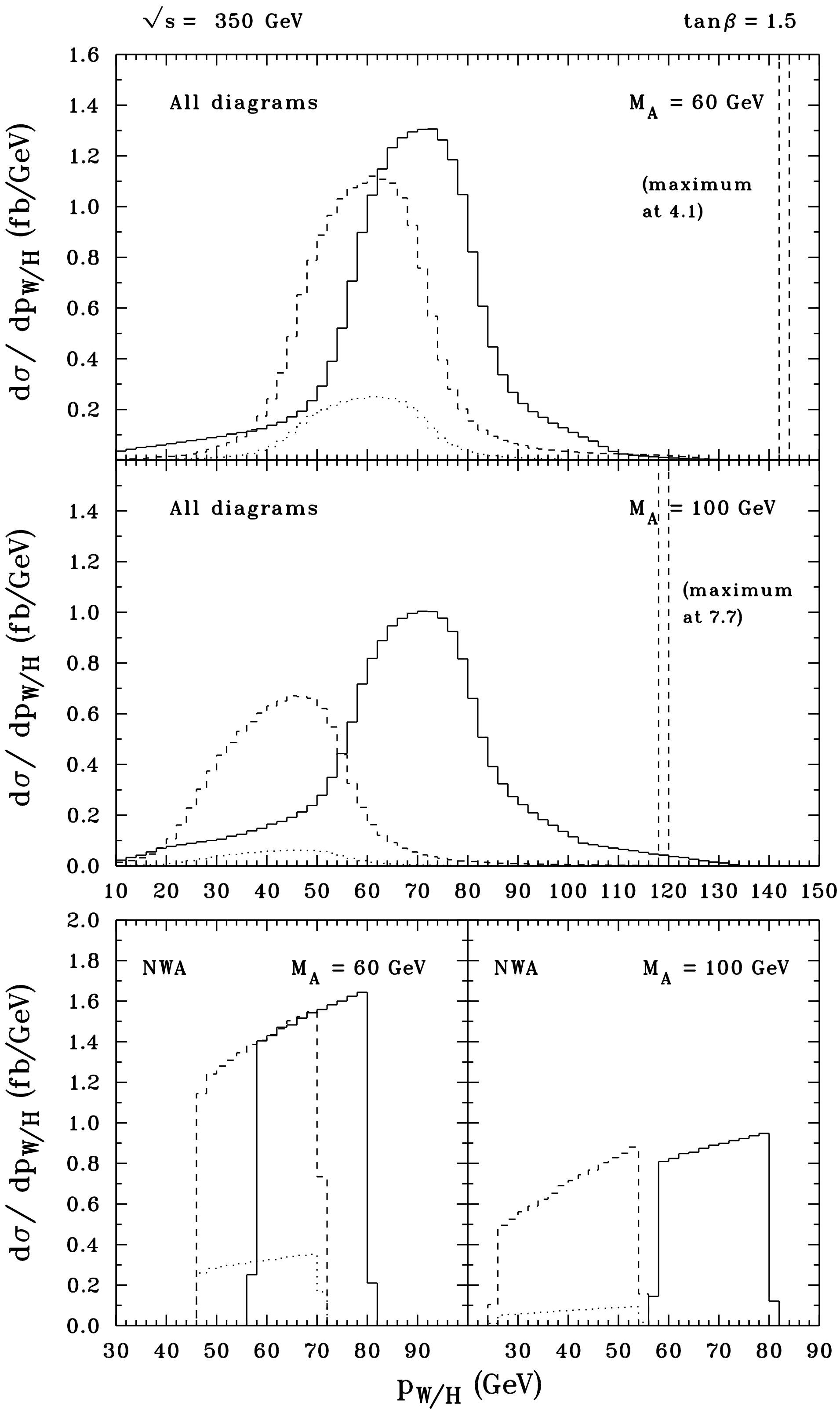

$\sqrt{s}$ = 350 GeV
tanβ = 1.5
All diagrams
M_A = 60 GeV
(maximum at 4.1)
All diagrams
M_A = 100 GeV
(maximum at 7.7)
NWA
M_A = 60 GeV
NWA
M_A = 100 GeV
$d\sigma/dp_{W/H}$ (fb/GeV)
$p_{W/H}$ (GeV)

Fig. 3a

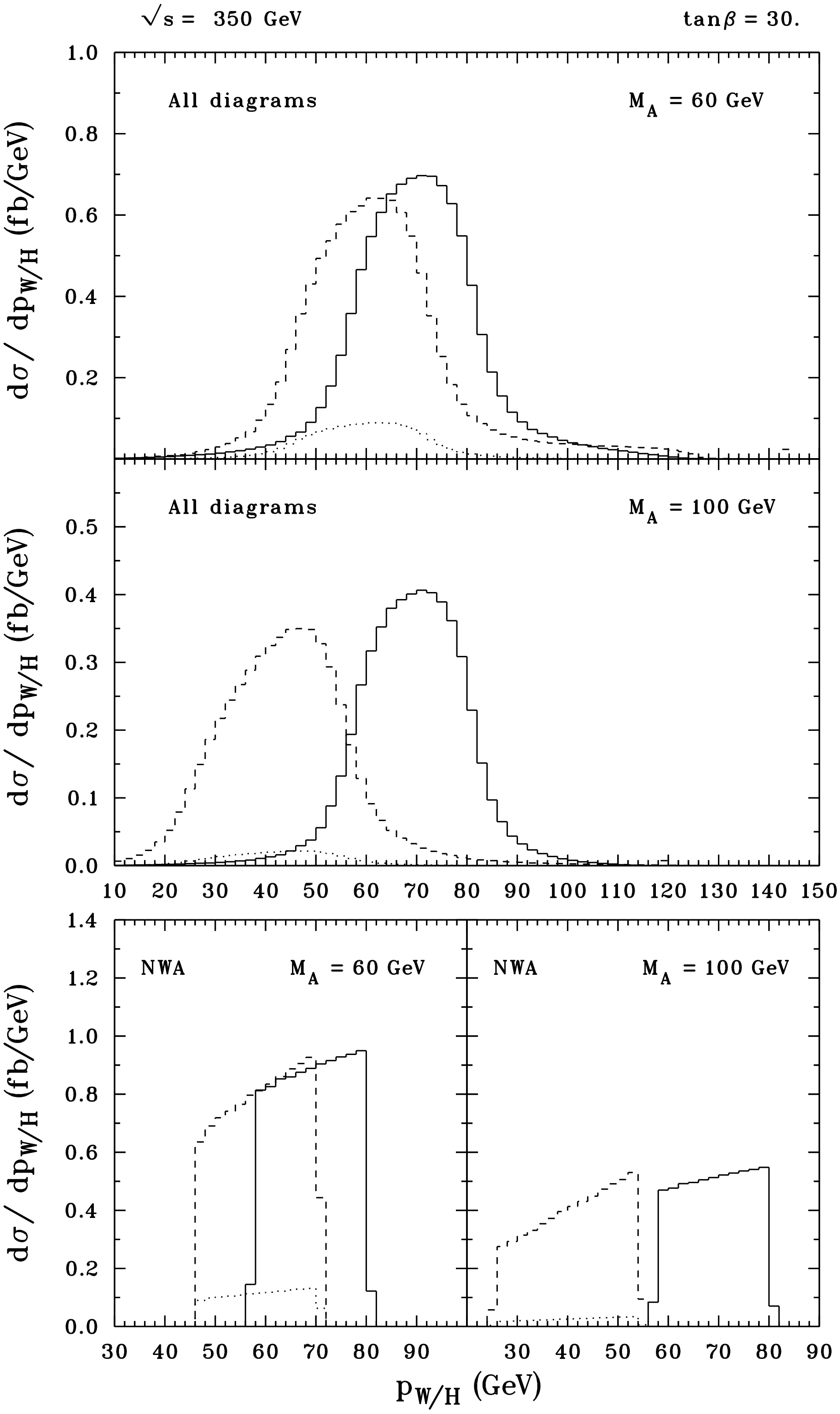

√s = 350 GeV
tanβ = 30.
All diagrams
M_A = 60 GeV
All diagrams
M_A = 100 GeV
NWA
M_A = 60 GeV
NWA
M_A = 100 GeV
dσ/ dp_W/H (fb/GeV)
p_W/H (GeV)

Fig. 3b

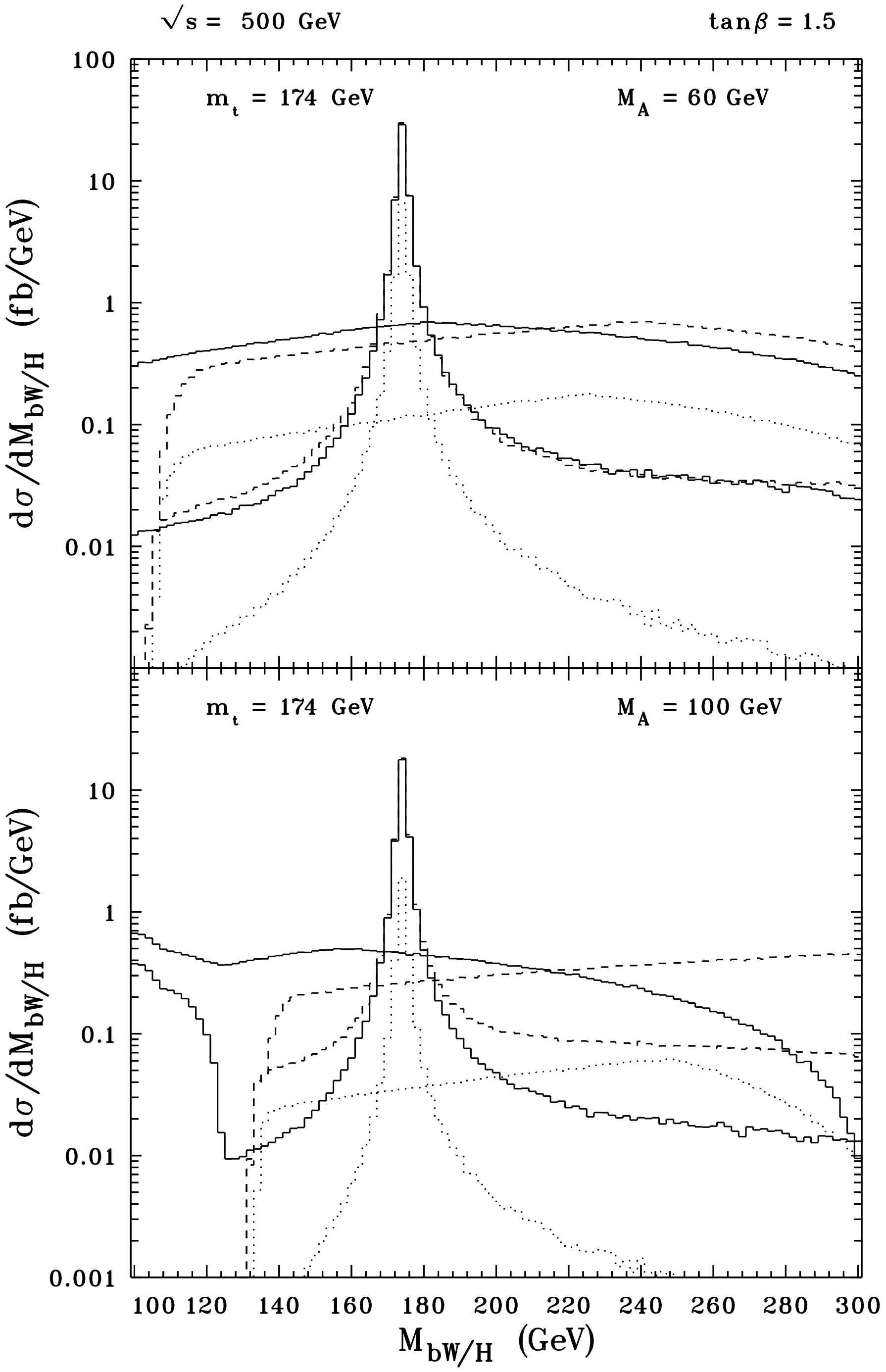

√s = 500 GeV
tanβ = 1.5
m_t = 174 GeV
M_A = 60 GeV
m_t = 174 GeV
M_A = 100 GeV
dσ/dM_bW/H (fb/GeV)
dσ/dM_bW/H (fb/GeV)
100
10
1
0.1
0.01
10
1
0.1
0.01
0.001
100 120 140 160 180 200 220 240 260 280 300
M_bW/H (GeV)

Fig. 4a

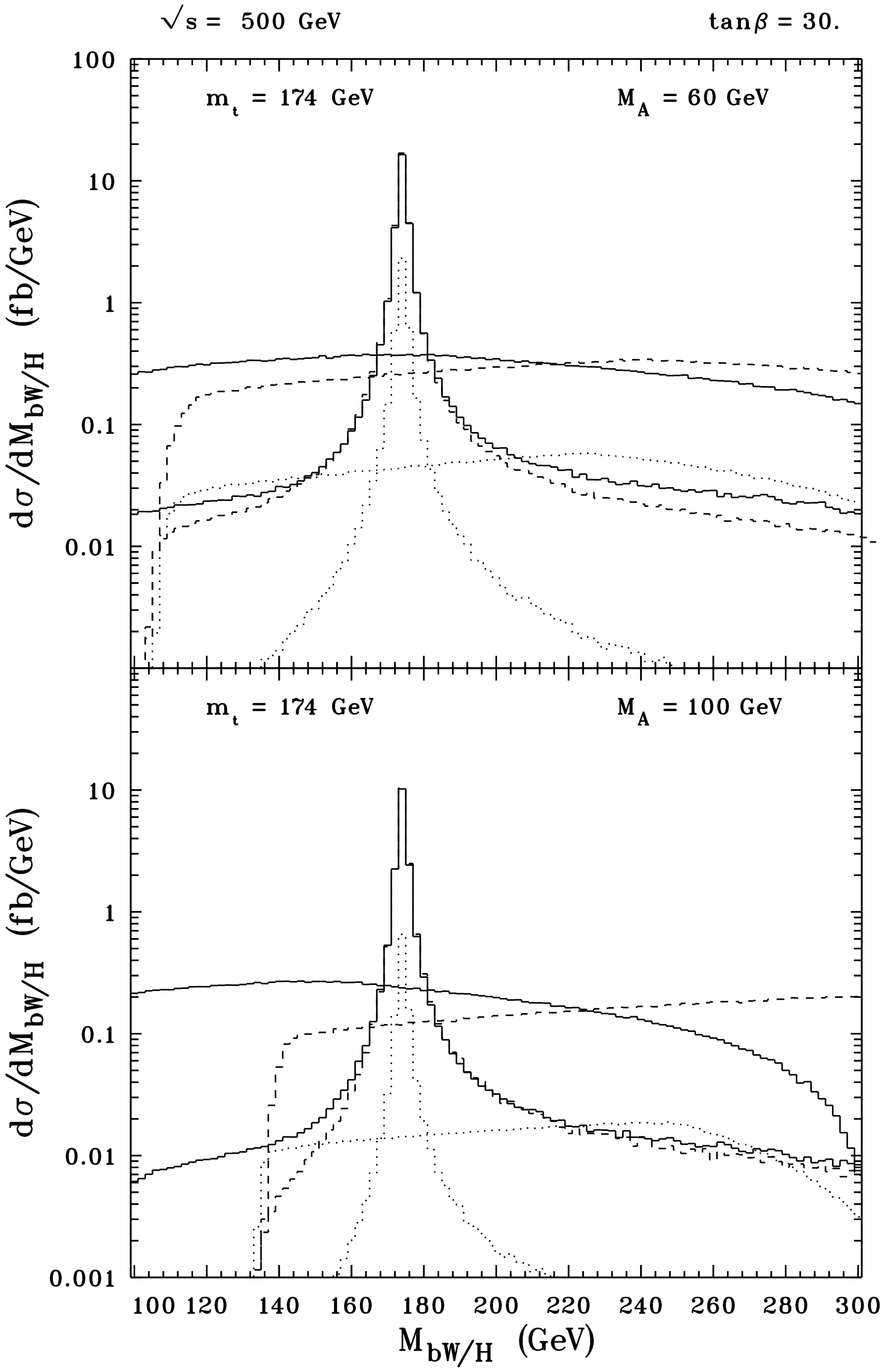

√s = 500 GeV
tanβ = 30.
m_t = 174 GeV
M_A = 60 GeV
M_A = 100 GeV
dσ/dM_bW/H (fb/GeV)
100
10
1
0.1
0.01
0.001
100 120 140 160 180 200 220 240 260 280 300
M_bW/H (GeV)

Fig. 4b

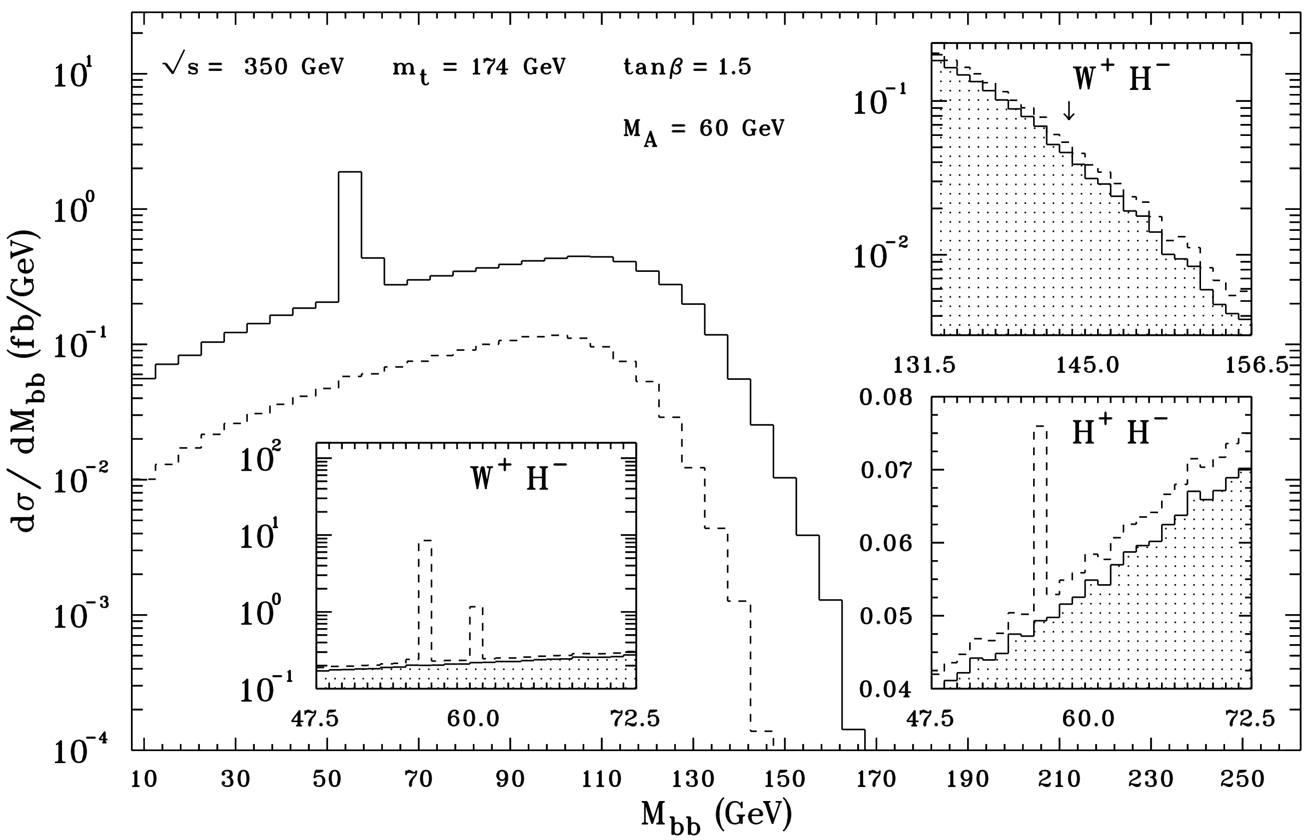

$\sqrt{s}$ = 350 GeV
m_t = 174 GeV
$\tan\beta$ = 1.5
M_A = 60 GeV
$d\sigma/dM_{bb}$ (fb/GeV)
M_{bb} (GeV)
$W^+ H^-$
$W^+ H^-$
$H^+ H^-$

Fig. 5a

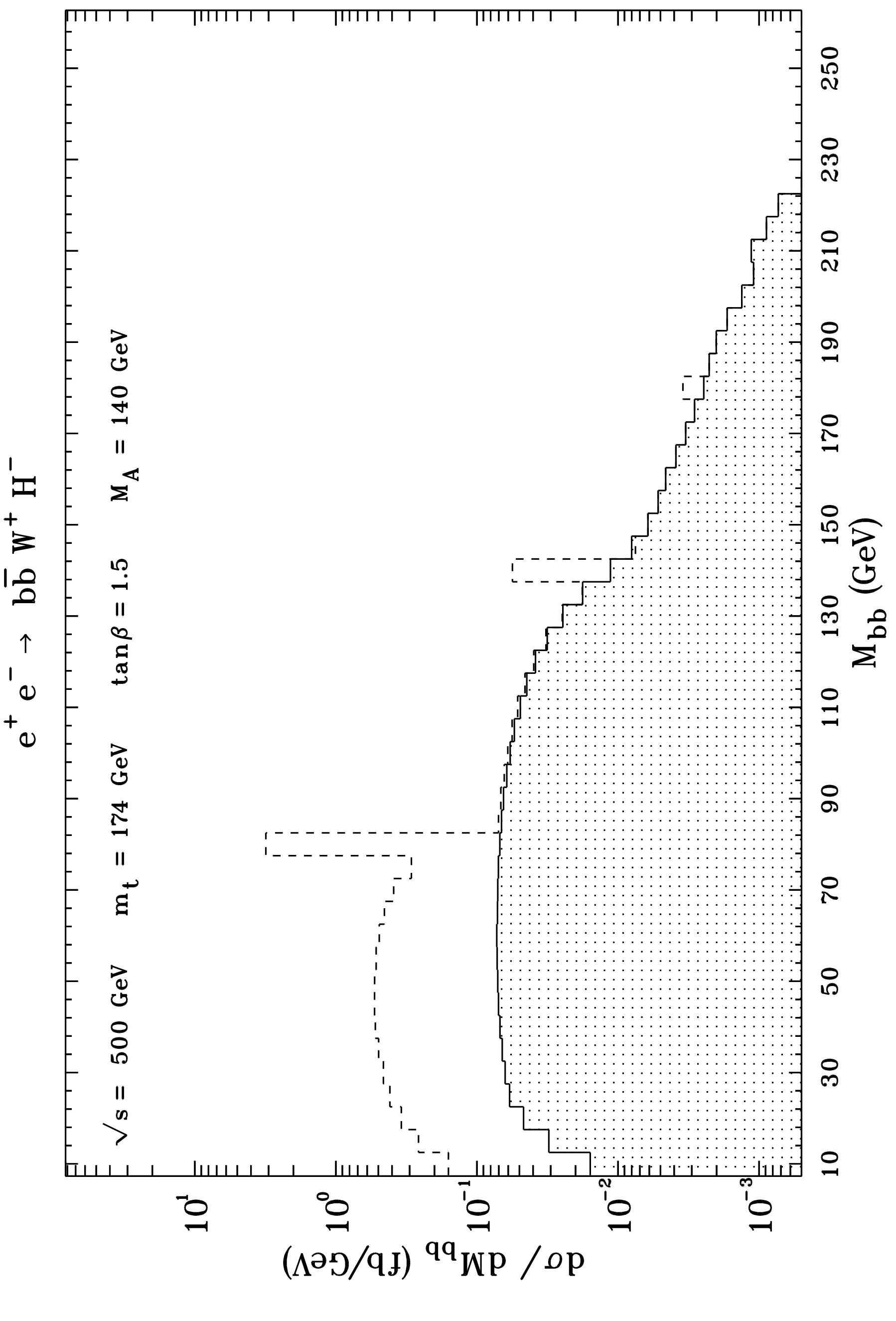

e+ e- → b b̄ W+ H-
√s = 500 GeV
m_t = 174 GeV
tanβ = 1.5
M_A = 140 GeV
dσ/ dM_bb (fb/GeV)
M_bb (GeV)

Fig. 5b

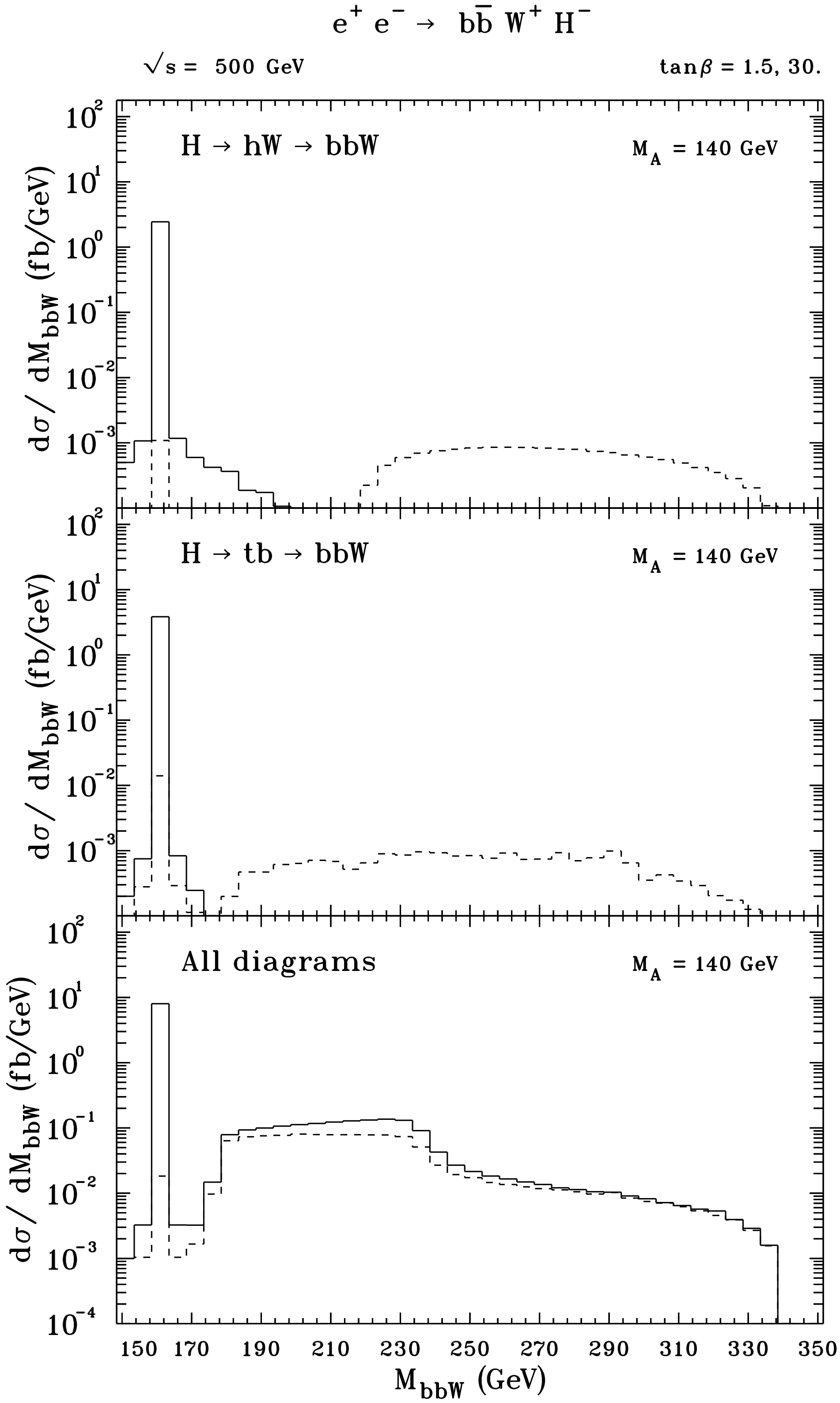

$e^+ e^- \to b\bar{b} W^+ H^-$
$\sqrt{s} =$ 500 GeV
$\tan\beta$ = 1.5, 30.
H → hW → bbW
M_A = 140 GeV
H → tb → bbW
M_A = 140 GeV
All diagrams
M_A = 140 GeV
$d\sigma / dM_{bbW}$ (fb/GeV)
10^2
10^1
10^0
10^{-1}
10^{-2}
10^{-3}
10^{-4}
150 170 190 210 230 250 270 290 310 330 350
M_{bbW} (GeV)

Fig. 6a

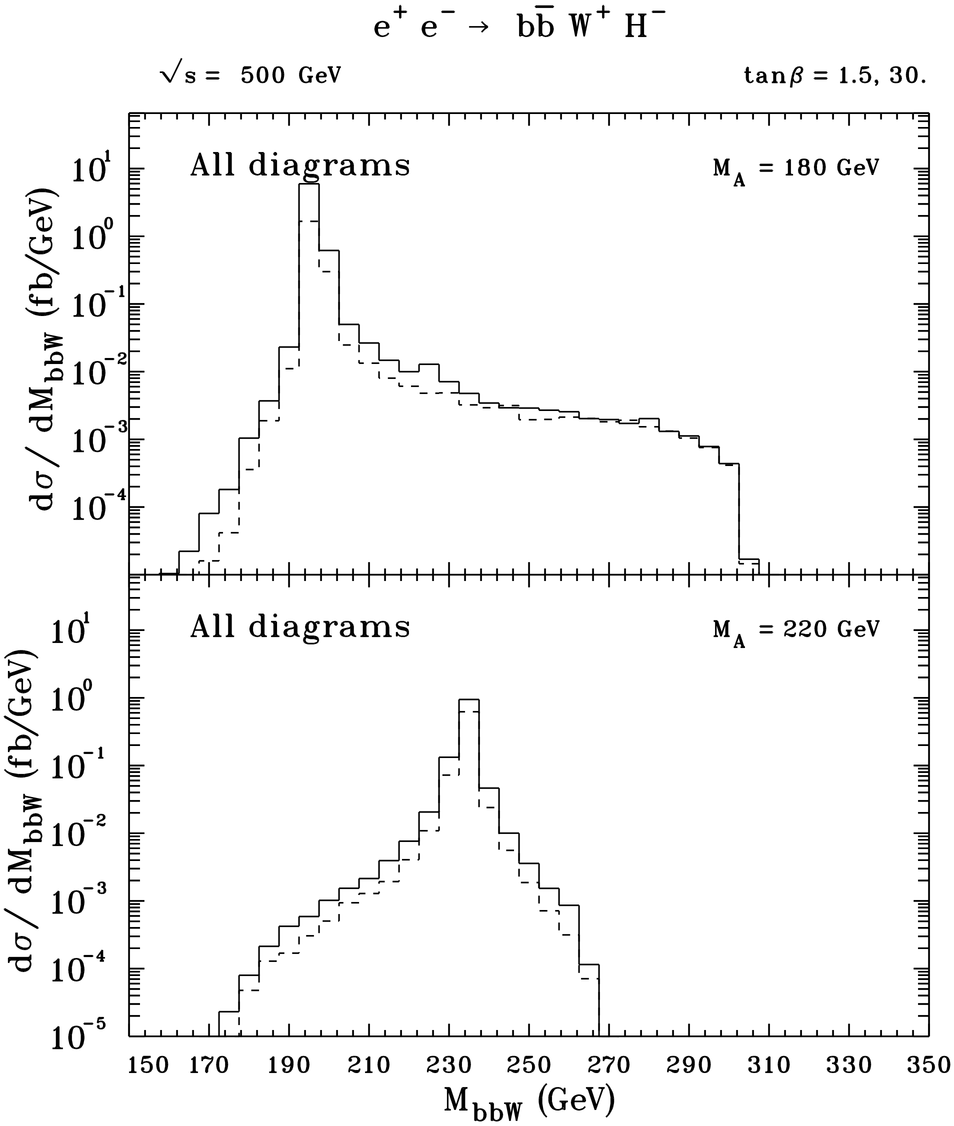
$e^+ e^- \to b\bar{b} W^+ H^-$
$\sqrt{s} =$ 500 GeV
$\tan\beta$ = 1.5, 30.
All diagrams
M_A = 180 GeV
All diagrams
M_A = 220 GeV
$d\sigma / dM_{bbW}$ (fb/GeV)
10^1
10^0
10^{-1}
10^{-2}
10^{-3}
10^{-4}
10^{-5}
150 170 190 210 230 250 270 290 310 330 350
M_{bbW} (GeV)

Fig. 6b

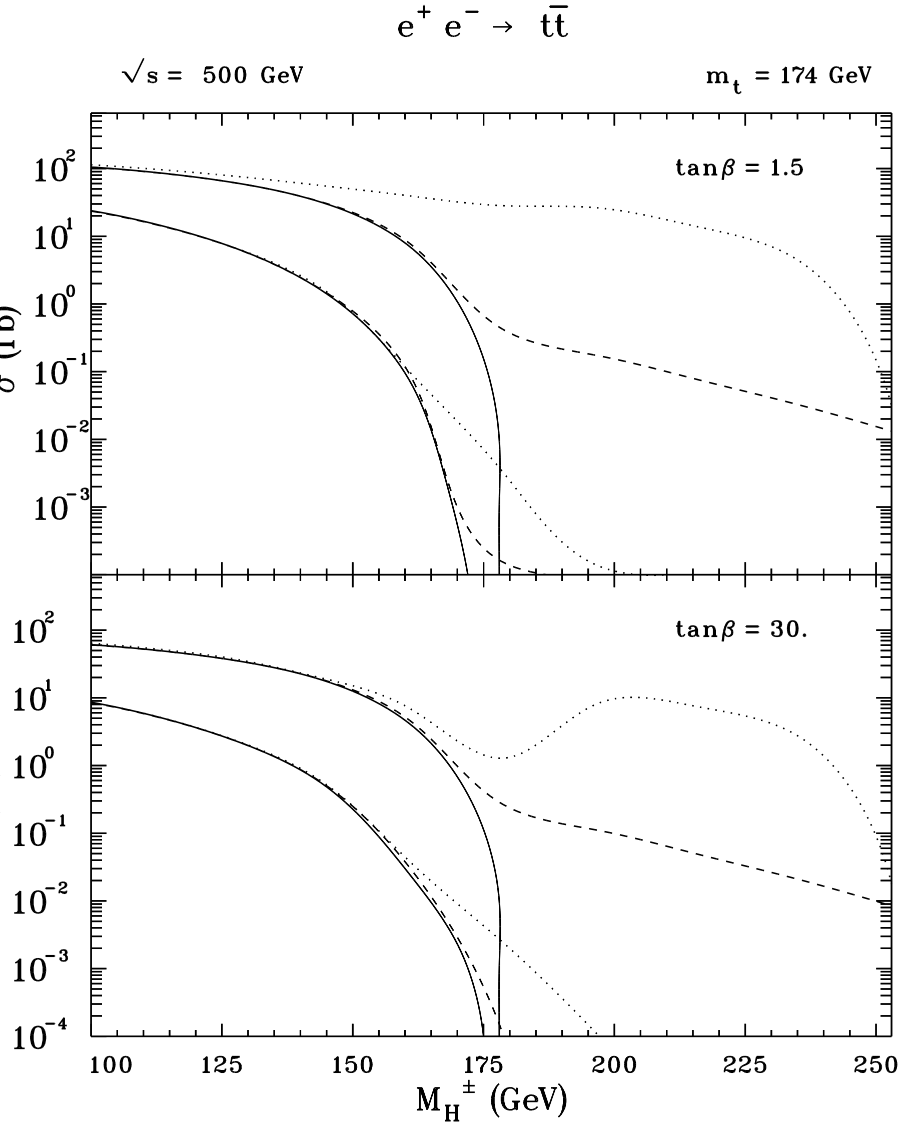

$e^+ e^- \to t\bar{t}$
$\sqrt{s}$ = 500 GeV
m_t = 174 GeV
$\tan\beta$ = 1.5
$\tan\beta$ = 30.
σ (fb)
σ (fb)
10^2
10^1
10^0
10^{-1}
10^{-2}
10^{-3}
10^{-4}
100
125
150
175
200
225
250
$M_{H^\pm}$ (GeV)

Fig. 7

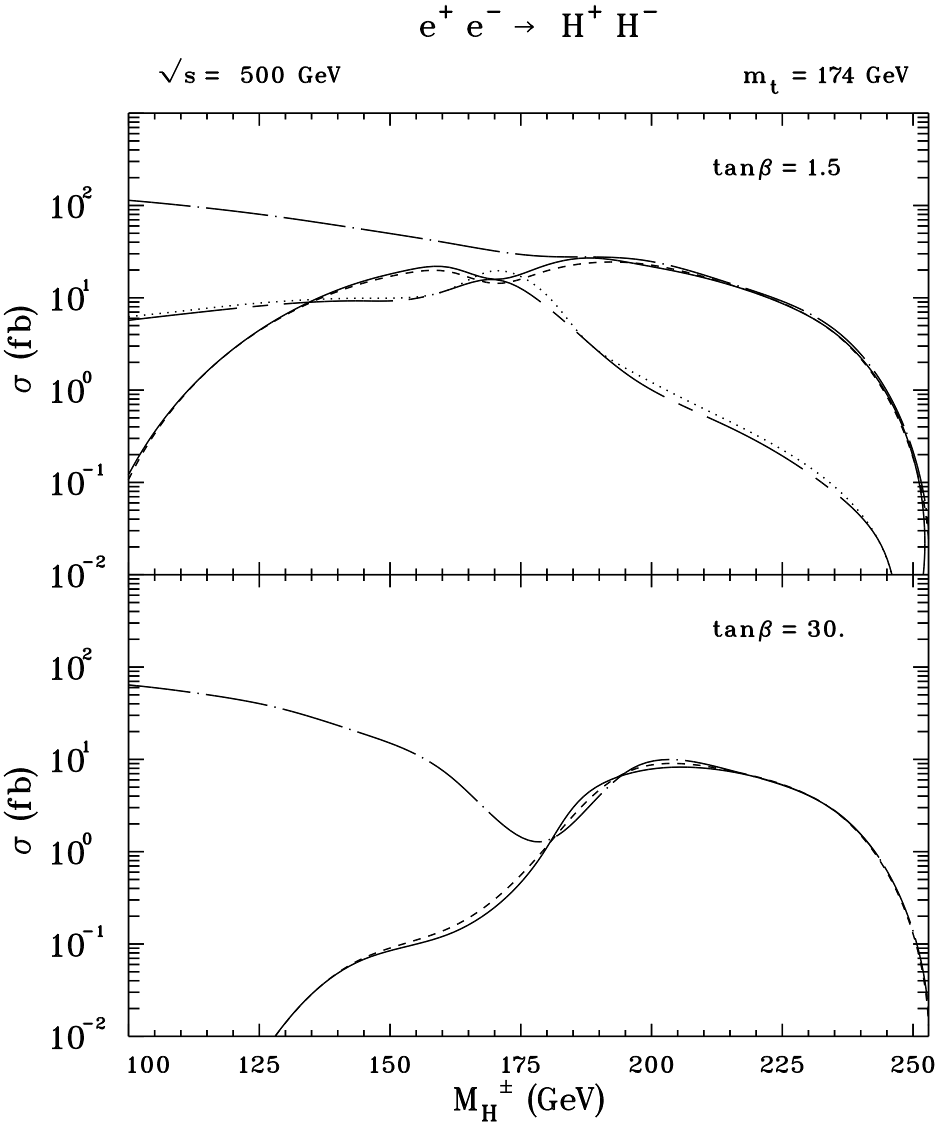

$e^+ e^- \to H^+ H^-$
$\sqrt{s}$ = 500 GeV
m_t = 174 GeV
tanβ = 1.5
tanβ = 30.
σ (fb)
10^2
10^1
10^0
10^{-1}
10^{-2}
100
125
150
175
200
225
250
$M_{H^\pm}$ (GeV)

Fig. 8